Global Change Biology

Global Change Biology (2016), doi: 10.1111/gcb.13348

Regional atmospheric cooling and wetting effect of permafrost thaw-induced boreal forest loss

MANUEL HELBIG[1], KAROLINE WISCHNEWSKI[1], NATASCHA KLJUN[2], LAURA E. CHASMER[3], WILLIAM L. QUINTON[4], MATTEO DETTO[5] and OLIVER SONNENTAG[1]

[1]*Département de géographie & Centre d'études nordiques, Université de Montréal, 520 Chemin de la Côte Sainte-Catherine, Montréal, QC H2V 2B8, Canada,* [2]*Department of Geography, Swansea University, Singleton Park, Swansea SA28PP, Swansea, UK,* [3]*Department of Geography, University of Lethbridge, 4401 University Drive, Lethbridge, AB T1K 3M4, Canada,* [4]*Cold Regions Research Centre, Wilfrid Laurier University, 75 University Ave. W, Waterloo, ON N2L 3C5, Canada,* [5]*Smithsonian Tropical Research Institute, Luis Clement Ave., Bldg. 401 Tupper, Balboa Ancon, Panama, Republica de Panama*

Abstract

In the sporadic permafrost zone of North America, thaw-induced boreal forest loss is leading to permafrost-free wetland expansion. These land cover changes alter landscape-scale surface properties with potentially large, however, still unknown impacts on regional climates. In this study, we combine nested eddy covariance flux tower measurements with satellite remote sensing to characterize the impacts of boreal forest loss on albedo, eco-physiological and aerodynamic surface properties, and turbulent energy fluxes of a lowland boreal forest region in the Northwest Territories, Canada. Planetary boundary layer modelling is used to estimate the potential forest loss impact on regional air temperature and atmospheric moisture. We show that thaw-induced conversion of forests to wetlands increases albedo, bulk surface conductance for water vapour and aerodynamic surface temperature. At the same time, heat transfer efficiency is reduced. These shifts in land surface properties increase latent at the expense of sensible heat fluxes, thus, drastically reducing Bowen ratios. Due to the lower albedo of forests and their masking effect of highly reflective snow, available energy is lower in wetlands, especially in late winter. Modelling results demonstrate that a conversion of a present-day boreal forest–wetland to a hypothetical homogeneous wetland landscape could induce a near-surface cooling effect on regional air temperatures of up to 3–4 °C in late winter and 1–2 °C in summer. An atmospheric wetting effect in summer is indicated by a maximum increase in water vapour mixing ratios of 2 mmol mol^{-1}. At the same time, maximum boundary layer heights are reduced by about a third of the original height. In fall, simulated air temperature and atmospheric moisture between the two scenarios do not differ. Therefore, permafrost thaw-induced boreal forest loss may modify regional precipitation patterns and slow down regional warming trends.

Keywords: boreal forest, climate change, eddy covariance, energy flux, evapotranspiration, land cover change, permafrost, wetland

Received 10 February 2016 and accepted 2 April 2016

Introduction

A large proportion of North America's high-latitude landscapes contain permafrost, perennially cryotic ground, spanning from the tundra in the north, over subarctic woodlands, to the boreal forests further south (Strong *et al*., 1989). About 60% of North America's boreal forests lie in the zones of discontinuous permafrost (50% to <90% of the land surface contains permafrost) and sporadic permafrost (10% to <50%) (e.g. Olson *et al*., 2001; van Everdingen, 2005; Gruber, 2012; Helbig *et al*., 2016). Across the circumpolar permafrost zone, rapid rates of climate warming are already occurring and are projected to intensify in the near future (Hartmann *et al*., 2013).

Correspondence: Manuel Helbig, tel. 438-826-1985, fax 514-343-8008, e-mail: manuel.helbig@umontreal.ca

Climate change is expected to alter the composition and structure of boreal forest and wetland ecosystems inducing strong biophysical and biogeochemical feedbacks to global and regional climates through altered land–atmosphere interactions (e.g. Chapin *et al*., 2000, 2005; Meissner *et al*., 2003; Bonan, 2008; Alkama & Cescatti, 2016). At high latitudes, biophysical feedbacks to regional climates mainly imply changes in the surface fluxes of sensible and latent heat (Bonan, 2008). Vegetation composition and structure strongly determine physical and biological land surface properties such as albedo, surface temperature, and bulk aerodynamic and surface conductance (Eugster *et al*., 2000; Kasurinen *et al*., 2014). Thus, vegetation changes alter surface properties and consequently also turbulent energy flux regimes (e.g. Snyder *et al*., 2004; Davin & de Noblet-Ducoudré, 2010; Baldocchi & Ma, 2013; Luyssaert *et al*.,

2014; Alkama & Cescatti, 2016). For example, a shift from deciduous to coniferous forests decreases surface conductance and increases the Bowen ratio, the ratio of sensible to latent heat flux (Eugster *et al.*, 2000). The modified diurnal heat input to the regional planetary boundary layer (PBL) leads to altered diurnal PBL growth dynamics affecting its effective heat capacity, entrainment of dry air from the free atmosphere, and, consequently, feedbacks to regional air temperatures and convective rainfall (e.g. Baldocchi *et al.*, 2000; Juang *et al.*, 2007a; Esau *et al.*, 2012). In addition, boreal forests exert a strong biophysical influence on regional air temperatures even at latitudes far outside their zone of distribution due to its effect on the general circulation of the atmosphere (Bonan *et al.*, 1992; Snyder *et al.*, 2004).

At the southern limit of the permafrost zone in Canada and Alaska, warming air temperatures cause widespread thaw. In recent decades, thaw-induced disappearance of forested permafrost plateaus has led to a conversion of boreal forests to wetlands (e.g. Camill & Clark, 1998; Camill, 1999a; Jorgenson *et al.*, 2001; Quinton *et al.*, 2011; Helbig *et al.*, 2016; Lara *et al.*, 2016). Permafrost plateaus dominated by coniferous tree species rooted in raised, thick organic soils, and treeless, seasonally frozen wetlands are the two predominant land cover types of the lowland boreal landscapes in the discontinuous and sporadic permafrost zones of north-western Canada (Zoltai & Tarnocai, 1975; Tarnocai, 2006). The proportional coverage of forests and wetlands is affected by the degree of permafrost thaw (Quinton *et al.*, 2011). Forested permafrost plateaus and wetlands differ in their soil moisture and temperature regimes with wetlands being substantially wetter and warmer (Chasmer *et al.*, 2011a; Quinton & Baltzer, 2013; Baltzer *et al.*, 2014; Fig. S1). In wetlands, root inundation and mortality inhibits tree growth, resulting in sharp forest-wetland transitions of vegetation composition and structure (e.g. Camill, 1999b; Baltzer *et al.*, 2014).

Despite the importance of boreal forests in the permafrost zone for the global and regional climates (Chapin *et al.*, 2000), local- to regional-scale responses of land–atmosphere interactions to thaw-induced land cover change are still poorly understood. It remains unclear as to how such vegetation shifts may affect turbulent energy fluxes and how these might modify regional trends in air temperature and atmospheric moisture. The biophysical consequences of permafrost thaw-induced boreal forest loss and ultimately disappearance have received little attention compared with deforestation in the temperate and tropical zones and wildfires in the boreal zone (e.g. Liu *et al.*, 2005; Randerson *et al.*, 2006). The impacts of disappearing permafrost on regional turbulent energy flux regimes need to be better constrained to project the trends of air temperature and atmospheric moisture in the boreal zone (Chapin *et al.*, 2000) and to evaluate the performance of current land surface schemes and terrestrial biosphere models (Fisher *et al.*, 2014). In this study, we aim to:

1 quantify the impact of permafrost disappearance and concurrent tree cover loss on turbulent energy fluxes,
2 identify the landscape-scale (~1 km^2) changes in land surface properties causing turbulent energy flux changes,
3 quantify boreal tree cover controls on land surface properties on a regional scale (~4000 km^2) and
4 estimate potential effects of thaw-induced shifts in land cover on regional air temperature and atmospheric moisture.

Materials and methods

Study site

Scotty Creek (61°18′N; 121°18′W, NT, Canada) is a 152-km^2 watershed located in the southern Taiga Plains and is situated in the zone of sporadic permafrost (Fig. 1a). The southern part of the watershed is characterized by rapidly thawing permafrost resulting in a mosaic of forested permafrost plateaus, wetlands, forested uplands and shallow thaw lakes (Chasmer *et al.*, 2014). Permafrost-free wetlands occur as collapse-scar bogs that receive some lateral inflow of water from the surrounding forests, and as channel fens that route water towards the watershed outlet (National Wetlands Working Group, 1997; Quinton *et al.*, 2009). Organic soils are widespread in the region with peat thickness ranging from 0.6 to 5 m (Aylsworth *et al.*, 1993). Black spruce (*Picea mariana*) is the dominant tree species on the forested permafrost plateaus. Understorey and ground cover on the permafrost plateaus mainly consist of Labrador tea (*Rhododendron groenlandicum*), ground lichen (*Cladonia* spp.), and *Sphagnum fuscum* and *capillifolium*. *Sphagnum balticum* and *magellanicum* and ericaceous shrubs mainly populate the collapse-scar bogs (Garon-Labrecque *et al.*, 2015).

The mean annual air temperature (1981–2010) in Fort Simpson, ca. 60 km north of Scotty Creek, is −2.8 °C with a mean

Fig. 1 (a) Location of the Scotty Creek watershed (surface elevation ~285 m a.s.l.), zones of sporadic (10% to <50% areal permafrost coverage), discontinuous (50% to <90%), and continuous (≥90%) permafrost (data from Gruber, 2012), and areal extent of the boreal and tundra zones (data from Olson *et al.*, 2001). (b) Per cent tree cover in 2010 in the southern Taiga Plains. Pixels with surface elevations <250 m a.s.l. and >300 m a.s.l. are shaded. (c) Land cover types in the vicinity of the two flux towers (Chasmer *et al.*, 2014) and their flux footprint climatologies for the period April to November 2014.

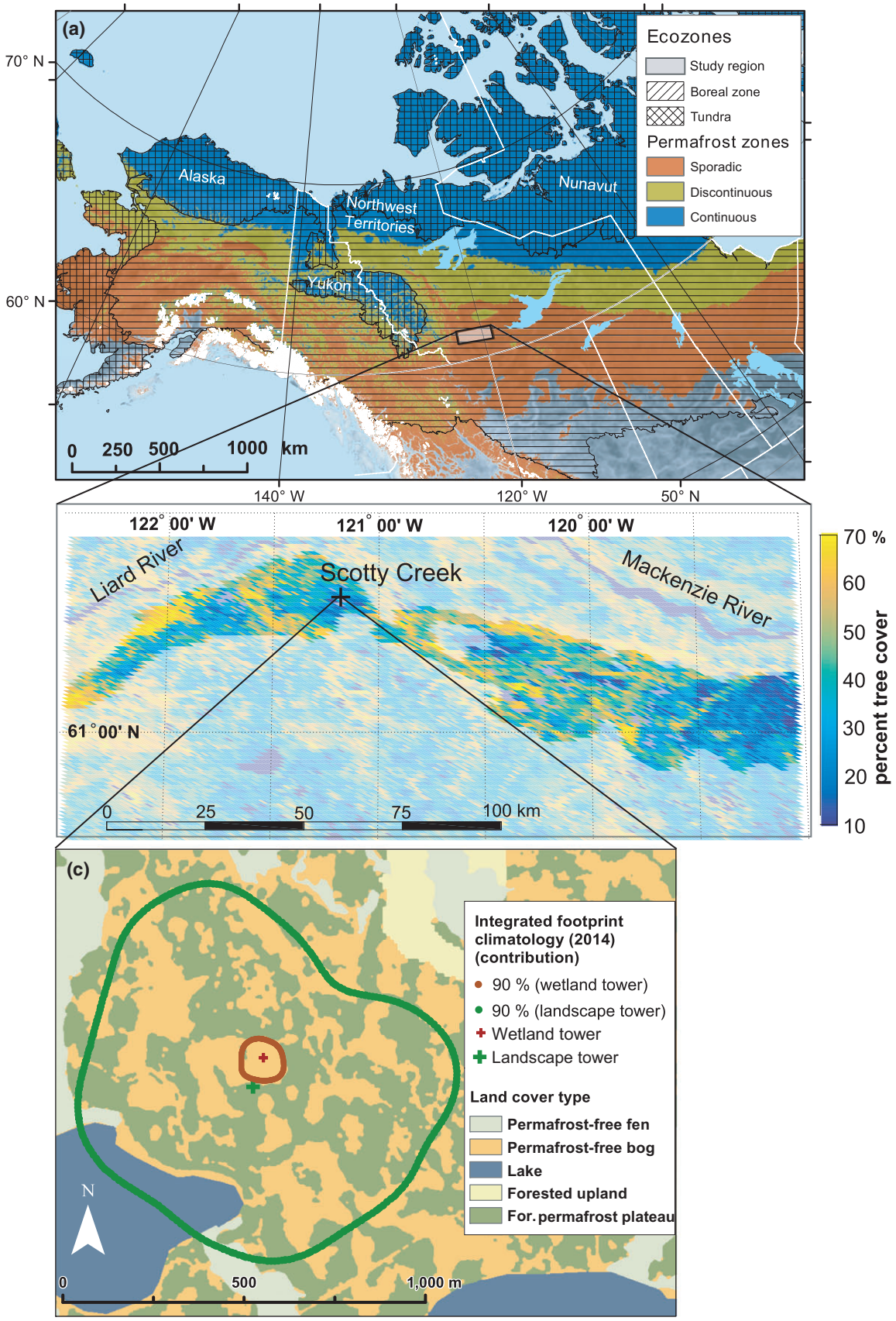

 Global Change Biology, doi: 10.1111/gcb.13348

January air temperature of −24.2 °C and a mean July air temperature of 17.4 °C. The long-term mean total annual precipitation (1981–2010) is 388 mm. Snowfall accounts for about 50% of the total annual precipitation. During the study period, from May to November 2013 and April to November 2014, mean air temperature was 2.1 and 0.2 °C warmer and total precipitation was 73 mm (26%) and 87 mm (29%) lower than the long-term average, respectively (Environment Canada, 2014).

Eddy covariance measurements

Turbulent momentum and energy fluxes were measured at Scotty Creek using the eddy covariance technique at two nested micrometeorological towers (Baldocchi, 2014). One eddy covariance system was mounted on top of a 15-m tower with flux footprints originating from a boreal forest–wetland landscape (hereafter referred to as 'landscape tower', measurement period: 11 May 2013 to 07 November 2014). A second system was installed on a 2-m tower in a wetland just north of the landscape tower at 1.9 m above the ground surface (hereafter referred to as 'wetland tower', measurement period: 12 April 2014 to 07 November 2014). Its flux footprints originated mainly from the wetland and were within the landscape tower flux footprint (Fig. 1c).

The eddy covariance instrumentation, identical at both towers, included a sonic anemometer (CSAT3A; Campbell Scientific Inc., Logan, UT, USA) and a CO_2/H_2O open-path infrared gas analyser (EC150; Campbell Scientific Inc.), both operating at 10-Hz frequencies. Friction velocity (u_*; m s^{-1}), sensible (H, W m^{-2}) and latent heat fluxes (LE, W m^{-2}) were computed using the EddyPro software (version 5.2, LI-COR Biosciences, Lincoln, NE, USA). For the landscape tower, a planar fit method was deployed to rotate the coordinate system of the sonic anemometer into the mean streamlines of the wind field (Wilczak *et al*., 2001). To account for small seasonal changes in the orientation of the sonic anemometer due to potential variations of the wetland surface, a double rotation method was applied for the wetland tower, so that the half-hourly mean vertical wind velocity equalled zero. Further corrections were applied to take into account spikes in the high-frequency time series (Vickers & Mahrt, 1997), humidity effects on sonic temperature (Van Dijk *et al*., 2004), block averaging of half-hour time series, time lag detection, spectral attenuation (Moncrieff *et al*., 1997, 2004), and air density fluctuations for water vapour fluxes (Webb *et al*., 1980).

Supporting measurements

Four-component net radiometers (CNR4, Kipp & Zonen, Delft, The Netherlands) at the landscape (at a height of 13.4 m) and the wetland (2.1 m) tower measured incoming and outgoing short- and long-wave radiation fluxes. Following Schmid (1997), the radiometric footprint (80% contour) at the landscape tower contained 77% forest with the remaining 23% being wetland. The radiometric footprint at the wetland tower consisted only of wetland. Therefore, the radiation fluxes at the landscape and the wetland tower were considered to represent forest and wetland surfaces, respectively. Air temperature and relative humidity probes (HC2-S3; Rotronic AG, Bassersdorf, Switzerland) were installed at 15 m and at 2.6 m at the landscape and the wetland tower, respectively. Soil heat flux at 8 cm below the moss surface at the forest and at the wetland was measured in a hummock and hollow using two ground heat flux plates (HFT3, Hukseflux, Delft, The Netherlands) at each site. To calculate soil heat storage between the heat flux plates and the moss surface, half-hourly changes in soil temperatures at 2, 4 and 8 cm below the surface (TCAV; Campbell Scientific Inc. and Type 'T'; Omega Engineering, Stamford, CT, USA) were used assuming a constant heat capacity of the peat above the heat flux plate of 2 MJ m^{-3} K^{-1} (Hayashi *et al*., 2007). Snow depth was measured in the forest and in the wetland using an ultrasonic distance sensor (SR50; Campbell Scientific Inc.). Snow density was measured on 10 days during late winter 2014 between 25 March and 22 April using a snow tube. Half-hour changes in snow depth, mean snow density and the latent heat of fusion of water were used to calculate the forest and wetland snow melt energy flux.

Footprint modelling

To resolve the spatial heterogeneity within the flux tower footprints, we ran the 2D footprint parameterization of Kljun *et al.* (2015) for both towers providing not only the extent but also the width of footprints. Similar to the model of Kljun *et al.* (2004), this parameterization is based on the Lagrangian particle dispersion footprint model of Kljun *et al.* (2002) and is valid for convective to stable boundary layer conditions. The footprint model was used to calculate the half-hourly per-grid cell flux contributions for a discretized study area. Roughness lengths for momentum (z_{0m}; m) and zero-plane displacement heights (d_0; m) for each half-hour were derived from high-frequency sonic anemometer data to account for the spatial heterogeneity in canopy height and geometry (see A1 and Supplementary material). The relative half-hourly flux contributions of each land cover type to the total flux were calculated as the weighted sum of the respective per-grid cell flux contributions. The 90% flux footprints of the landscape tower mainly contained a mix of wetlands and forests, while the wetland tower predominantly contained surfaces from one ecosystem, the wetland (Fig. 1c).

Postprocessing of eddy covariance measurements

A three-class quality flag system (Mauder & Foken, 2011) was used to remove half-hourly periods that do not meet steady-state conditions or when turbulence was not fully developed. Remaining outliers were filtered using a spike detection algorithm (Papale *et al*., 2006). To ensure the comparability between flux measurements at the landscape and the wetland tower, we assessed their energy balance closures (EBC). The EBC was 0.79 and 0.78 for the landscape and the wetland tower, respectively, after removing wetland tower fluxes with <95% wetland contribution and applying a u*-threshold filter (u^* = 0.2 m s^{-1}). (see A2). These EBC values are in good

agreement with Stoy *et al*. (2013) who reported a mean EBC of 0.76 ± 0.13 and of 0.88 ± 0.23 for seven wetlands and 47 evergreen needle-leaf forest sites, respectively.

Experimental errors in eddy covariance measurements are a combination of systematic and random errors (Moncrieff *et al*., 1996). The potential systematic error derived from the EBC analysis (~20%) does not hamper the comparability of H and LE between the two towers, assuming that the EBC residuals are similarly attributed to H and LE for the landscape and the wetland tower. Maximum instrument-specific systematic errors in LE are estimated to be ±8% based on an intercomparison study of the open-path EC150 with closed-path infrared gas analysers (M. Helbig, K. Wischnewski, G. H. Gosselin, S. C. Biraud, I. Bogoev, W. S. Chan, E. S. Euskirchen, A. J. Glenn, P. M. Marsh, W. L. Quinton, O. Sonnentag, unpublished results).

Random half-hourly errors in H and LE were estimated as the standard deviation of H and LE for similar meteorological conditions and flux footprints within a time window of ±7 days (Lasslop *et al*., 2008). These random errors were used in regression analyses after York *et al*. (2004), accounting for errors in both the dependent and the independent variables. Mean random errors were 16.3 and 9.1 W m^{-2} in H, and 12.2 and 14.5 W m^{-2} in LE for the landscape and the wetland tower, respectively, and increased with the magnitude of both fluxes (Fig. S5).

Landscape-scale surface properties

Albedo and radiometric surface temperature represent two surface properties that are sensitive to changes in ecosystem structure and composition (e.g. Betts & Ball, 1997; Juang *et al*., 2007b; Lee *et al*., 2011), thus strongly affecting land–atmosphere interactions (e.g. Betts *et al*., 2001). Tower-based radiation measurements over the wetland (2014) and over the forest (2013 and 2014) were used to assess the effects of thaw-induced forest loss on landscape-scale albedo and radiometric surface temperature. Aerodynamic surface properties, such as bulk aerodynamic conductance for heat and water vapour (g_H; m s^{-1}; see Supplementary material) and bulk surface conductance for water vapour (g_s; m s^{-1}), were derived using Monin–Obukhov similarity theory (Garratt, 1994; Betts *et al*., 1999). We derived aerodynamic surface temperature (T_{as}; K) of the flux footprints from measured H and modelled g_H using the following bulk transfer relationship:

$$H = \rho C_p g_H (T_{as} - T_a) \quad (1)$$

where ρ is air density [kg m^{-3}], C_p is the heat capacity of air [J kg^{-1} K^{-1}], and T_a is air temperature [K].

Aerodynamic surface temperature directly controls the turbulent heat exchange between land surface and overlying atmosphere. Thus, T_{as} differs from radiometric surface temperature, which represents a weighted soil and canopy temperature as function of viewing angle of the thermal-infrared radiometer mounted on tower platforms (Detto *et al*., 2006; Kustas *et al*., 2006) or satellite platforms (Wan, 2014).

Similarly, we obtained a bulk formulation for LE by assuming the same bulk aerodynamic conductance as for sensible heat (g_H) and by adding a bulk surface conductance term, g_s (Betts *et al*., 1999):

$$LE = \lambda \left(\frac{g_H g_s}{g_H + g_s} \right) [q_s(T_{as}) - q_a] \quad (2)$$

where λ is the latent heat of vapourization [J kg^{-1}], q_s is the saturated specific humidity of air at T_{as} [kg kg^{-1}], and q_a is the specific humidity of air at measurement height [kg kg^{-1}].

Increasing wetland coverage in the boreal forest–wetland landscape may affect the response of g_s to variations in vapour pressure deficit (VPD; kPa) and incoming short-wave radiation (SW_{in}; W m^{-2}). We applied a boundary line analysis by fitting nonlinear VPD and SW_{in} models to the upper boundary of half-hourly g_s for three flux footprint classes of increasing wetland contribution (e.g. Grelle *et al*., 1999; Igarashi *et al*., 2015): a 'low wetland class' with footprint contributions from wetlands <63%, a 'medium wetland class' with contributions from wetlands between 63% and 95%, and a 'high wetland class' with contributions from wetlands >95% (i.e. from the wetland tower). Only the maximum g_s in each VPD and SW_{in} bin (G_{s_bound}; m s^{-1}) were selected to minimize reductions in g_s due to other environmental drivers (see A3).

Regional-scale patterns of albedo and radiometric surface temperature

To assess regional effects of permafrost thaw-induced tree cover loss on albedo and radiometric surface temperature (T_{rs}; K), we analysed several MODIS satellite products for a ~4000-km^2 area of interest in the southern Taiga Plains (Fig. 1b). These products included per cent tree cover from the annual MOD44B Vegetation Continuous Field product, white-sky albedo from the 16-day MCD43B3 Albedo product, and daytime and night-time T_{rs} from the 8-day MOD11A2 Land Surface Temperature/Emissivity product for the years 2000–2015. White-sky albedo does not account for the direct radiative component and is therefore not a function of solar angle and atmospheric conditions, making it suitable for the assessment of albedo variations due to changes in surface characteristics (Schaepman-Strub *et al*., 2006; Jin *et al*., 2012).

Surface elevation from the MODIS Geolocation product (MOD03) was used to mask pixels with elevations below 250 m a.s.l. and above 300 m a.s.l. to minimize altitudinal effects on T_{rs} (e.g. Li *et al*., 2015). Scotty Creek is located at 285 m a.s.l. Pixels classified as open water bodies by the MODIS Land Water Mask (MOD44W) were discarded from the analysis. We only analysed white-sky albedo and T_{rs} pixels with good-quality flags and with error flags indicating an average T_{rs} error ≤3 K. To remove thermal anomalies in T_{rs} due to wildfires, we masked all pixels identified as active fires by the MODIS Thermal Anomalies & Fire product (MOD14A1). All data sets were resampled to a spatial resolution of 1 km^2.

Planetary boundary layer modelling

The potential impact of a conversion of the present-day heterogeneous boreal forest–wetland to a hypothetical

homogeneous permafrost-free, treeless wetland landscape on potential air temperature (θ_m; K) and water vapour mixing ratio (q_m; mol mol^{-1}) in the PBL was assessed with a clear-sky PBL model (McNaughton & Spriggs, 1986; Baldocchi & Ma, 2013; see A4). We ran the PBL model using u_*, H and LE from the landscape (representing a present-day heterogeneous landscape with permafrost) and the wetland tower (as a proxy for a hypothetical homogeneous permafrost-free landscape) and compared the diurnal θ_m and q_m dynamics. The model inputs H and LE were corrected for the observed lack of EBC maintaining the Bowen ratio (Twine *et al.*, 2000). To illustrate diurnal θ_m and q_m dynamics for the two scenarios, we analysed modelled θ_m and q_m for one clear-sky day in the summer with no gaps in the model input time series (22 June 2014: 0800 - 2100 Mountain Standard Time (MST)). The mean footprint contributions for the landscape tower fluxes on that day were 40% from wetlands, 56% from forested peat plateaus and 4% from the lake. These contributions are representative for the present-day landscape in the southern part of the Scotty Creek watershed that consisted of 57 ± 8% and 52 ± 9% forested permafrost plateaus in 2000 and 2010, respectively (Baltzer *et al.*, 2014). Additionally, we ran the PBL model for a total of 49 days between 15 May 2014 and 08 October 2014 and derived daily θ_m and q_m differences between the two landscape scenarios at 1800 MST (see A4 for selection criteria for modelled days). We compared PBL dynamics as observed over the present-day boreal forest–wetland landscape to a hypothetical permafrost-free wetland landscape. However, complete disappearance of permafrost likely enhances large-scale drainage conditions (e.g. Connon *et al.*, 2014). The current conditions at the studied wetland site may therefore not be directly representative of a future, potentially drier, permafrost-free boreal landscape. Hence, the modelled absolute changes in θ_m and q_m should be seen as an upper limit.

Results

Changes in turbulent energy fluxes

At the end of winter in May 2014, a frost layer with a maximum depth of about 80 cm was observed in the wetland (Fig. S1). The mean water table between April and November 2014 was 15 cm below the moss surface. In contrast, a maximum thawed layer of 40 cm overlaid cryotic soil between May and September 2014 in the forest and the decrease in water table level closely followed thaw depth during the summer. In 2014, the snow melt at the forest and the wetland occurred at the end of April and the ground was snow-covered again in October (Fig. S1). During the snow cover period in late winter, half-hourly H at the wetland tower (H_{WET}) was negative most of the time, while H at the landscape tower (H_{LAND}) already reached maximum values of 200 W m^{-2} (Fig. 2a). At the same time, the largest mean midday (1200 – 1500 MST) Bowen ratio was observed for the landscape tower with 7.6 ± 0.8 (±95% CI of mean), while the mean midday Bowen ratio at the wetland tower was the lowest with −0.3 ± 0.3 (Fig. 2c). Between May and November 2014, H_{WET} amounted to about 50% of H_{LAND} and the ratio of the two fluxes approached unity with higher contributions of

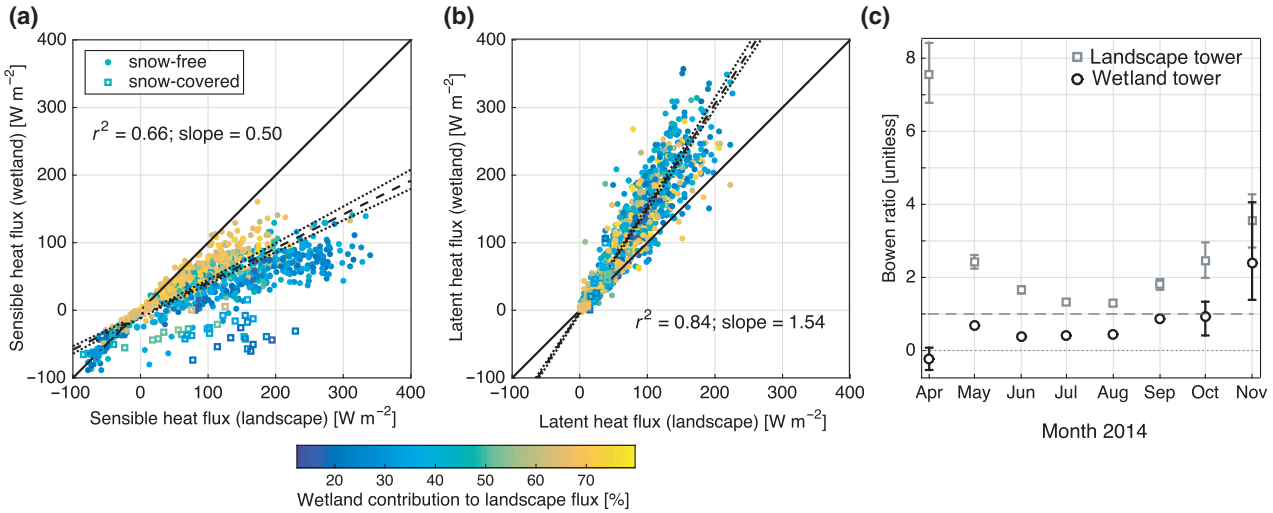

Fig. 2 (a) Turbulent sensible and (b) latent heat fluxes at the landscape (over a boreal forest–wetland landscape) and at the wetland tower (over a permafrost-free wetland) between 12 April and 07 November 2014. Colours of dots indicate relative contributions of wetlands to landscape tower fluxes. Best-fit lines with errors in both variables (York *et al.*, 2004) for the snow-free period are indicated as black dashed lines and slopes were significant at α = 0.001. Dotted black lines indicate 95% confidence intervals (CI) of the regression as derived from 1000 bootstrap simulations of the data. (c) Monthly mean midday (1200–1500 MST) Bowen ratio (sensible heat flux/latent heat flux) for the landscape and the wetland tower. Error bars indicate the 95% CI of the means.

wetlands in the landscape tower footprints (Fig. 2a, slope of H_{LAND} against H_{WET} increased significantly from 0.47 to 0.64 [$P < 0.001$ two-sample non-parametric Kolmogorov-Smirnov test] for H_{LAND} with wetland contributions ≤36% (25th percentile) versus ≥63% (75th). In contrast, half-hourly *LE* at the wetland tower (LE_{WET}) was about 54% larger than *LE* at the landscape tower (LE_{LAND}, Fig. 2b). Slopes of LE_{LAND} against LE_{WET} were closer to unity with increasing contributions of wetlands to LE_{LAND} (slope decreased significantly from 1.63 to 1.47 [$P < 0.001$] for LE_{LAND} with wetland contributions ≤36% vs. ≥63%). Monthly mean midday Bowen ratios in the snow-free period ranged from 1.3 in July to 2.5 in October and from 0.4 in June to 0.9 in October at the landscape and the wetland tower, respectively (Fig. 2c). The total half-hourly turbulent energy flux ($H + LE$) was 13% smaller at the wetland tower compared to the landscape tower (slope = 0.87, $r^2 = 0.86$).

Changes in surface properties

Albedo. Albedo determines how much short-wave radiation is reflected at the surface and, therefore, partly controls the available energy to generate *H* and *LE*. Between April and November 2014, the wetland albedo was consistently higher than the forest albedo, except for a 3-day period (28–30 April 2014) shortly after snow melt when the wetland was flooded (Fig. S2). Maximum albedo differences of 0.5 were observed during the snow cover period (April and October – November 2014). During the snow-free period, the wetland albedo exceeded the forest albedo by about 0.1. The regional median albedo (2000 – 2015; ~4000 km^2) in the southern Taiga Plains (Fig. 1b) showed similar seasonal dynamics as the albedo measured at the two towers. Median per cent tree cover of the region was 35% (2.5% percentile: 9%, 97.5% percentile: 69%). The forest albedo at Scotty Creek corresponded to the values at the lower end of the distribution of regional albedo, whereas the wetland albedo was consistently higher than the 95% confidence interval (except for the flooded period, Fig. 3).

Aerodynamic conductance. The median bulk aerodynamic conductance for heat (g_H) was 37.8 mm s^{-1} (2.5% percentile: 15.8 mm s^{-1}, 97.5% percentile: 69.8 mm s^{-1}) for the landscape and 23.7 mm s^{-1} (2.5% percentile: 16.6 mm s^{-1}, 97.5% percentile: 40.8 mm s^{-1}) for the wetland tower. Differences between g_H at the landscape and the wetland tower decreased with increasing wetland contributions to the landscape fluxes (Fig. 4). Median-weighted LiDAR-derived canopy height (see A1) within the flux footprints was 2.0 m (2.5% percentile: 1.1 m, 97.5% percentile: 3.7 m) and 0.3 m (2.5% percentile: 0.1 m, 97.5% percentile: 0.4 m) for the landscape and the wetland tower, respectively. Surface roughness length (z_0) increased linearly with the mean weighted LiDAR-derived canopy height ($r^2 = 0.75$, $P < 0.001$) and wetland contributions to flux footprints ($r^2 = 0.57$, $P < 0.001$; Fig. S3).

Aerodynamic surface temperature. A surface cooling effect of wetlands is indicated by increasingly warmer T_{as} of the landscape tower footprints (T_{as_LAND}) with decreasing wetland contributions compared to T_{as} of the

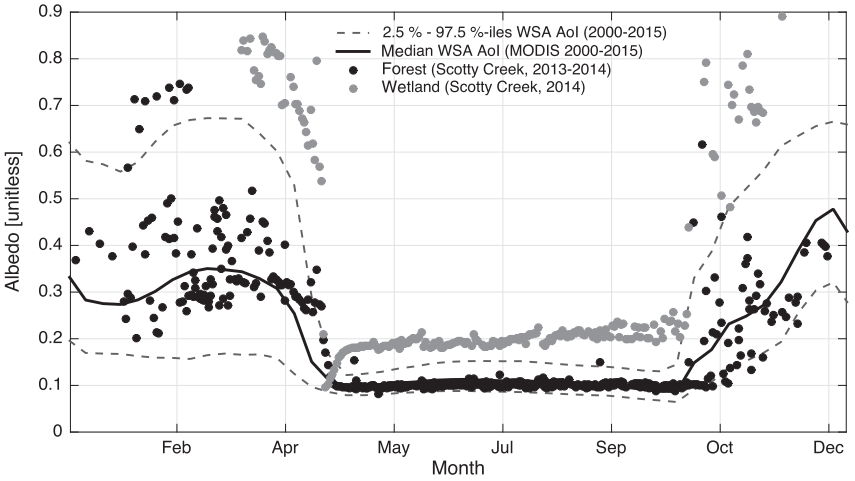

Fig. 3 Daily albedo of a boreal forest on a permafrost plateau (black dots, 2013–2014) and an adjacent permafrost-free wetland (grey dots, 2014), derived from four-component net radiometers at 1200 MST, and median (solid line, 2000–2015) and 2.5% percentile and 97.5% percentile (dotted lines) of 8-day 1-km white-sky albedo (WSA) across a ~4000 km^2 area of interest (AoI) in the southern Taiga Plains (derived from MCD43B3). Percentiles show spatial variability across the AoI.

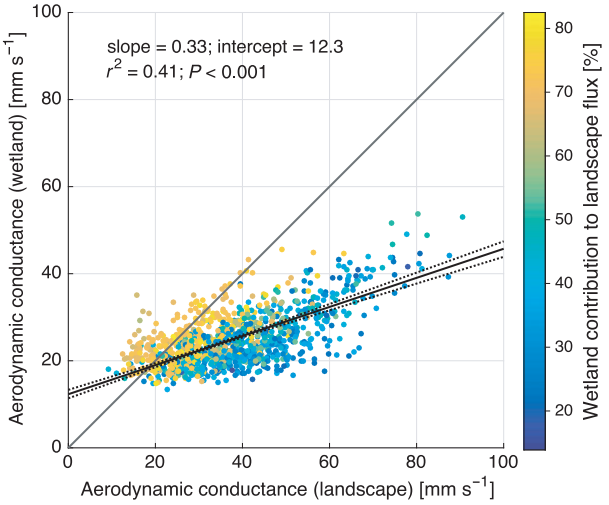

Fig. 4 Bulk aerodynamic conductance for heat in the footprints of the landscape and wetland tower. Colours of dots indicate contributions of wetlands to landscape tower fluxes. The total least-squares regression fit is shown as a solid black line. Dotted black lines indicate the 95% confidence interval of the regression as derived from 1000 bootstrap simulations of the data.

wetland (T_{as_WET}). The strongest cooling effect of 0.08 K per per cent wetland contribution (K %$^{-1}$) was observed for the snow cover period (Fig. 5a). During the snow-free period, wetland cooling ranged from 0.02 to 0.06 K %$^{-1}$ and coefficients of determination between differences in T_{as_LAND} and T_{as_WET} and wetland contributions to landscape fluxes increased from 0.10 in May to 0.24 in September (Figs. 5b–g). Both, daytime and night-time T_{as_LAND}, were warmer than T_{as_WET} during the snow cover period. During the snow-free period, night-time T_{as_LAND} was consistently warmer than T_{as_WET}, whereas daytime T_{as_LAND} was at times colder than T_{as_WET} (Fig. 5).

Surface conductance. In May and June 2013 and 2014, maximum bulk surface conductance (g_{s_0}; G_{s_bound} at a VPD of 0 kPa, see A3) increased from 7.2 mm s^{-1} (Fig. 6a and Table 1) for the 'low wetland class' to 34.5 mm s^{-1} for the 'high wetland class'. In late summer, a similar increase was observed, but g_{s_0} for the high wetland class was reduced to 18.0 mm s^{-1}. The sensitivity of G_{s_bound} to VPD ($G_{s\_bound} = g_{s\_0}\, e^{(-b_d\ VPD)}$; see A3) was most pronounced for the 'high wetland class' for May and June with the slope parameter b_d being 0.57 kPa^{-1}, whereas the 'medium wetland class' had the strongest sensitivity of G_{s_bound} to VPD between July and August with a b_d of 0.48 kPa^{-1}. The 'low wetland class' was the least sensitive during both periods (Table 1 and Fig. 6).

The limit of G_{s_bound} at infinite SW_{in} (g_{s_max} in $G_{s\_bound} = g_{s\_max}\ [SW_{in}/(b_{infl} + SW_{in})]$; see A3)

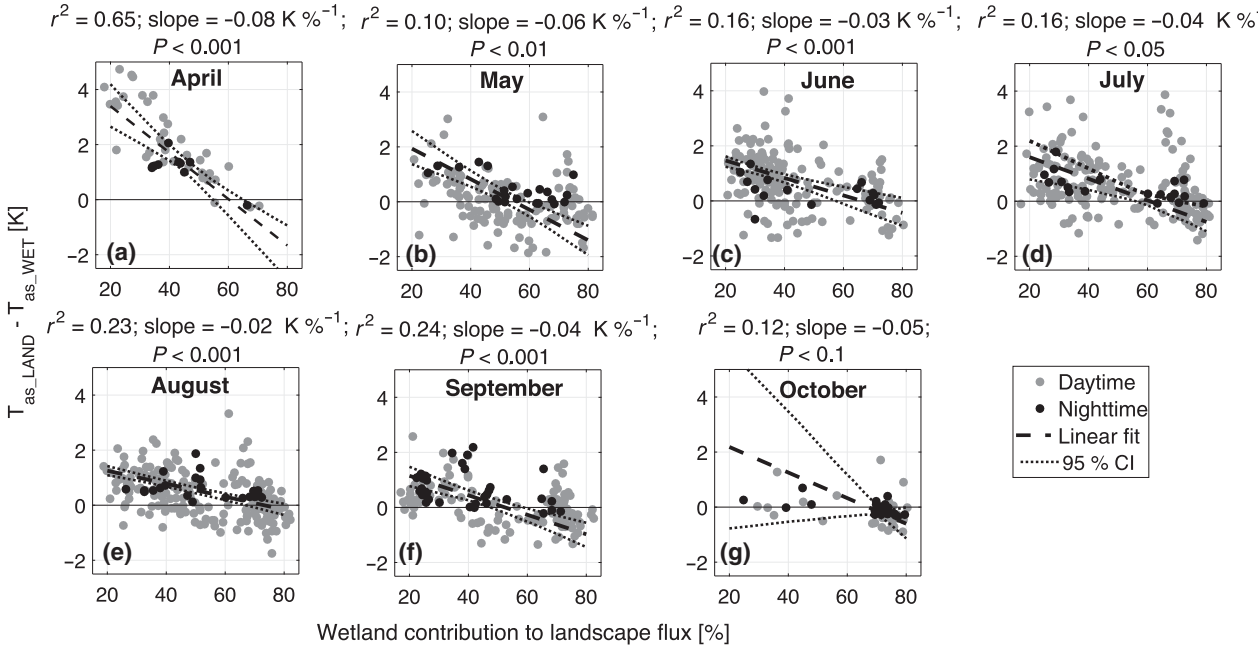

Fig. 5 Differences between aerodynamic surface temperatures of the landscape (T_{as_LAND}) and the wetland tower flux footprints (T_{as_WET}) as a function of wetland contributions to the landscape tower fluxes between April and October 2014. Daytime (grey dots) and night-time (black dots) differences are shown separately. Night-time is defined as periods with <50 W m^{-2} incoming short-wave radiation. Best-fit lines with errors in both variables (York *et al.*, 2004) are shown as dashed lines. Dotted lines indicate the 95% confidence intervals of best-fit lines as derived from 1000 bootstrap simulations of the data.

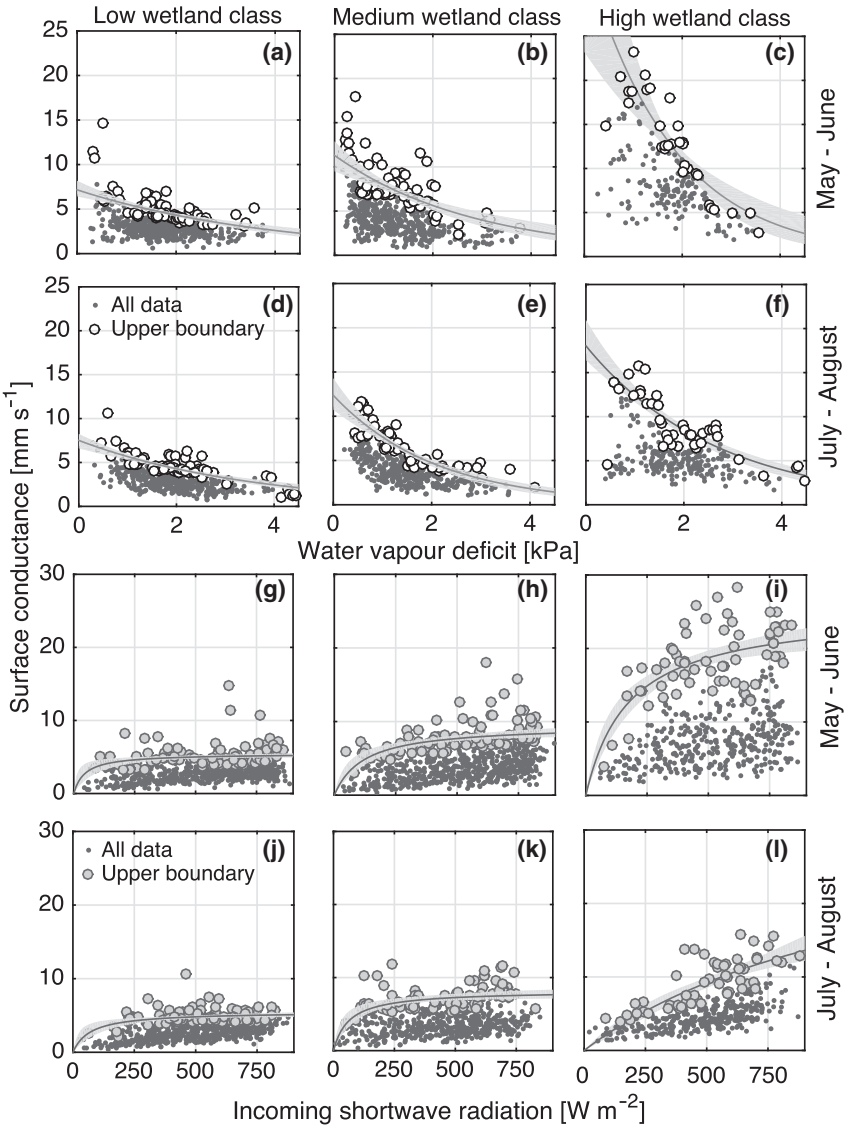

Fig. 6 Response of bulk surface conductance to (a–f) vapour pressure deficit and (g–l) incoming short wave radiation for the periods (a–c and g–i) May and June and (d–f and j–l) July and August for three classes of increasing permafrost-free wetland contributions ('low', 'medium', 'high'). Nonlinear model fits to the upper 15% of bulk surface conductance per 0.5 kPa (white circles) and 100 W m^{-2} bins (grey circles) are shown as solid lines. 95% confidence intervals are shown as shaded areas.

increased with increasing flux footprints contributions from wetlands peaking in July and August at 33.8 mm s^{-1}. The inflection point of the G_{s_bound} vs. SW_{in} relationship (b_{infl} [W m^{-2}], see A3) ranged between 45.8 W m^{-2} and 1337.2 W m^2 and was always highest for the 'high wetland class'. However, b_{infl} between classes were not significantly different, except for b_{infl} for the 'high wetland class' for July–August, which was significantly higher (Table 1). In July and August, g_{s_max} and b_{infl} were poorly constrained for the 'high wetland class' with 95% CI of 138.1 mm s^{-1} and 7531.4 W m^{-2}, respectively (Fig. 6).

Regional-scale controls on surface properties in the lowlands of the southern Taiga Plains

To assess the regional-scale relationships between tree cover and daytime and night-time T_{rs} and albedo, we analysed 1-km MODIS per cent tree cover, T_{rs}, and white-sky albedo between 2000 and 2015 for the southern Taiga Plains (Fig. 1b). The strongest relationships between daytime and night-time T_{rs} and tree cover were observed for March and April with r^2 of 0.34 and 0.27, respectively (Fig. 7a). During the night, areas with high tree cover were characterized by warmer T_{rs}

throughout the year with maximum T_{rs} sensitivities to tree cover of 0.08 K %$^{-1}$ in late winter. During the snow-free period (May to November), sensitivities were smaller with about 0.01 K %$^{-1}$ (expressed as increase in K per one per cent tree cover). Similarly, during the day, T_{rs} increased with tree cover during the winter

Table 1 Best parameter estimates and their 95% confidence intervals (CI) for vapour pressure deficit ($G_{s\_bound} = g_{s\_0}\, e^{(-b_d\ VPD)}$) and an incoming short-wave radiation models ($G_{s\_bound} = g_{s\_max}\,[SW_{in}/(b_{infl} + SW_{in})]$) of the upper boundary of bulk surface conductance (G_{s_bound}) for the periods May–June and July–August and for three classes of increasing permafrost-free wetland contribution to flux footprints. G_{s_bound} at a vapour pressure deficit of 0 kPa is given by g_{s_0}, while b_d is a slope parameter. G_{s_bound} at infinite short-wave incoming radiation is given by g_{s_max}, while b_{infl} is the inflection point (i.e. indicates the radiation value at which half of g_{s_max} is reached)

	Vapour pressure deficit (VPD) model				Incoming short-wave radiation (SW_{in}) model			
Wetland class	g_{s_0} [mm s^{-1}]	95% CI	b_d [kPa^{-1}]	95% CI	g_{s_max} [mm s^{-1}]	95% CI	b_{infl} [W m^{-2}]	95% CI
	May–June							
Low	7.2	6.4–8.2	0.25	0.19–0.32	5.5	5.1–6.1	45.8	12.2–107.1
Medium	11.3	9.5–12.9	0.35	0.23–0.45	9.6	8.4–10.9	120.6	51.8–197.1
High	34.5	23.2–53.1	0.57	0.36–0.80	25.3	22.0–29.4	175.4	96.7–279.3
	July–August							
Low	7.5	6.6–8.3	0.28	0.22–0.33	5.5	4.9–6.2	71.4	20.6–144.7
Medium	12.4	10.7–14.3	0.48	0.39–0.59	8.2	7.4–9.3	63.1	28.8–113.5
High	18.0	16.4–21.0	0.38	0.32–0.46	33.8	20.2–158.3	1337.2	567.8–8099.2

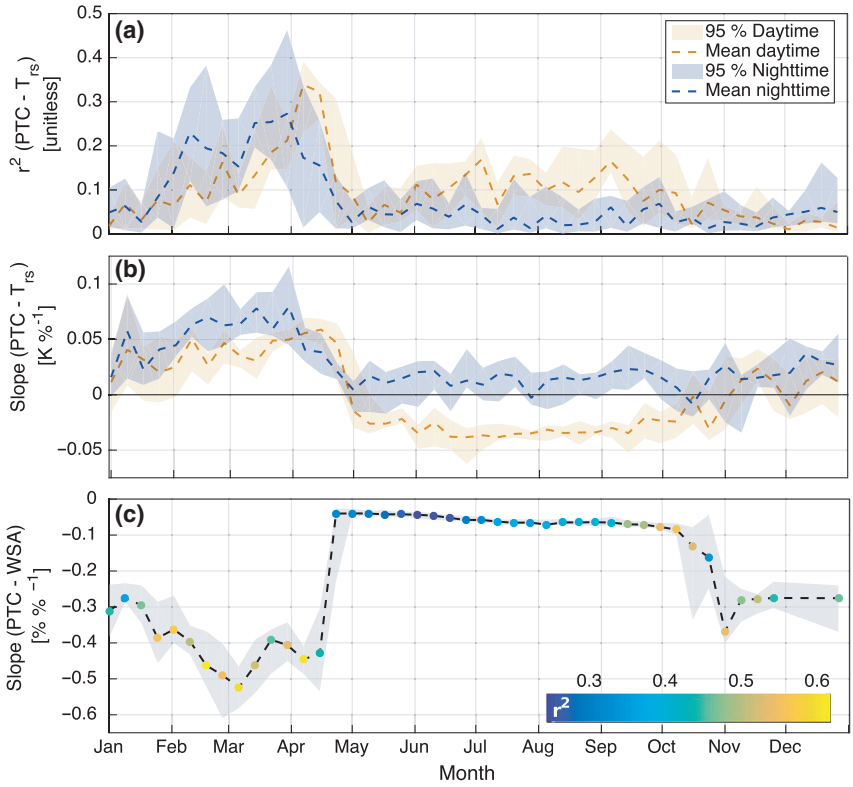

Fig. 7 (a) Seasonal dynamics of mean coefficients of determination (r^2) between 1-km per cent tree cover (PTC; MODIS VCF MOD44B) and 1-km daytime and night-time radiometric surface temperature (T_{rs} at about 1230 and 0030 MST, respectively; MODIS Land Surface Temperature/Emissivity MOD11A2) for a ~4000 km^2 area in the southern Taiga Plains. (b) Seasonal dynamics of mean slopes of the regression between PTC and T_{rs_rad}. (c) Seasonal dynamics of mean slopes between PTC and white-sky albedo (WSA, MODIS Albedo MOD43A3). Colours of dots represent mean r^2. Shaded areas indicate the 95% confidence intervals of the means for the period 2000–2015. All slopes are significant at $\alpha = 0.001$.

(November to April) peaking at 0.06 K $\%^{-1}$ in mid-April. In contrast, high tree cover areas were characterized by colder T_{rs} compared to areas with low tree cover during the snow-free period (negative slopes of up to −0.04 K $\%^{-1}$, Fig. 7b).

The strongest relationships between T_{rs} and tree cover in late winter coincided with the strongest relationship between tree cover and albedo (maximum slope of −0.55% $\%^{-1}$ in March; $r^2 = 0.62$; Fig. 7c). In April, slopes and r^2 between tree cover and albedo rapidly decreased and remained small until September before they gradually increased again to a slope of −0.38 % $\%^{-1}$ and an r^2 of 0.36 in early November (Fig. 7c).

In comparison, tower-based T_{rs} for the forest and wetland during the snow-free period indicate that median T_{rs} of the forest was 0.5 K colder during the day (1030 MST) and 1.7 K warmer during the night (2230 MST) (Fig. S4). During late winter, just before snow melt (13–30 April 2014), median daytime and nighttime T_{rs} of the forest was consistently warmer than T_{rs} of the wetland with differences of 1.2 and 1.8 K, respectively (Fig. S4).

Permafrost thaw-induced boreal forest loss effects on regional air temperature and atmospheric moisture

To estimate the potential effects of permafrost thaw-induced boreal forest loss on air temperature and atmospheric moisture, we modelled diurnal dynamics of PBL height, θ_m, and q_m for 49 clear-sky days in 2014 for two scenarios: a present-day heterogeneous boreal forest–wetland landscape ('present-day landscape') and a hypothetical homogeneous, permafrost-free, treeless wetland landscape ('permafrost-free landscape'). Results for one clear-sky day (22 June 2014) are discussed in detail.

Clear-sky conditions are usually characterized by a smooth diurnal curve of SW_{in} as observed on 22 June 2014 (Fig. 8a). *Heat* flux for the present-day scenario peaked at 1300 MST. In comparison, the sensible heat flux for the permafrost-free scenario was consistently smaller and peaked at 1200 MST. For the permafrost-free scenario, *LE* was larger than the present-day scenario *LE* between 1000 MST and 2030 MST and was slightly smaller during the morning hours (Fig. 8a).

Modelled θ_m fitted measured θ_m with a RMSE of 0.7 °C, while modelled q_m had a RMSE of 0.7 mmol mol^{-1}. The present-day scenario was warmer and drier than the permafrost-free scenario with differences of 2.0 °C in θ_m and 1.9 mmol mol^{-1} in q_m just before the PBL collapsed (Fig. 8b, c).

The PBL height was consistently larger for the present-day scenario compared to the permafrost-free scenario with differences of up to around 600 m. The mean effective heat capacity of the PBL for the present-day scenario was 52% higher. For the present-day and the permafrost-free scenario, 35% and 54% of the total sensible heat input was entrained with warm air from above the mixed layer. The total sensible heat input from the entrainment layer was 27% larger for the permafrost-free scenario just before the collapse of the PBL, mainly due to an enhanced gradient for this scenario between θ_m and potential temperature of the entrainment layer. The entrainment of dry air exceeded the surface input of water vapour for the present-day scenario causing a gradual q_m decrease during the day. For the permafrost-free scenario, the entrainment of dry air exceeded the water vapour input from the surface until 1430 MST. Afterwards, q_m gradually increased as the surface water vapour input (*LE*) exceeded the entrainment of dry air.

The largest mean differences in θ_m between the present-day and the permafrost-free scenario were observed during April 2014 when θ_m in the permafrost-free scenario were 3.6 ± 2.4 °C (± one standard deviation; $n = 3$) colder. During the summer, the permafrost-free scenario was 1.25 ± 0.8 (May and June; $n = 22$) and 1.58 ± 0.9 °C (July and August; $n = 16$) colder. In September, θ_m for the permafrost-free and the present-day scenario were similar with differences of 0.02 ± 1.4 °C ($n = 8$). Water vapour mixing ratios were higher for the permafrost-free scenario throughout the observation period with maximum differences in July and August of 2.06 ± 1.3 mmol mol^{-1}. The permafrost-free scenario was 1.42 ± 1.2 mmol mol^{-1} wetter in May and June and only marginally wetter in April and September with 0.30 ± 0.2 and 0.17 ± 0.9 mmol mol^{-1}, respectively.

Discussion

Permafrost thaw impacts on turbulent energy fluxes

Permafrost thaw-induced boreal forest loss in the sporadic permafrost zone accelerates and actively changes vegetation composition and structure (e.g. Baltzer *et al.*, 2014; Helbig *et al.*, 2016; Lara *et al.*, 2016). However, little is known about the biophysical impacts of these changes on local- to regional-scale land–atmosphere interactions. Insights from global climate models are limited by their spatial resolution (Oleson *et al.*, 2004). Remote sensing allows biophysical impact assessment of deforestation on climate (e.g. surface and air temperature) across the globe (Li *et al.*, 2015; Alkama & Cescatti, 2016) whereas *in situ* eddy covariance measurements in combination with local-scale modelling are useful to gain in-depth understanding of the underlying ecosystem processes (Juang *et al.*, 2007a,b;

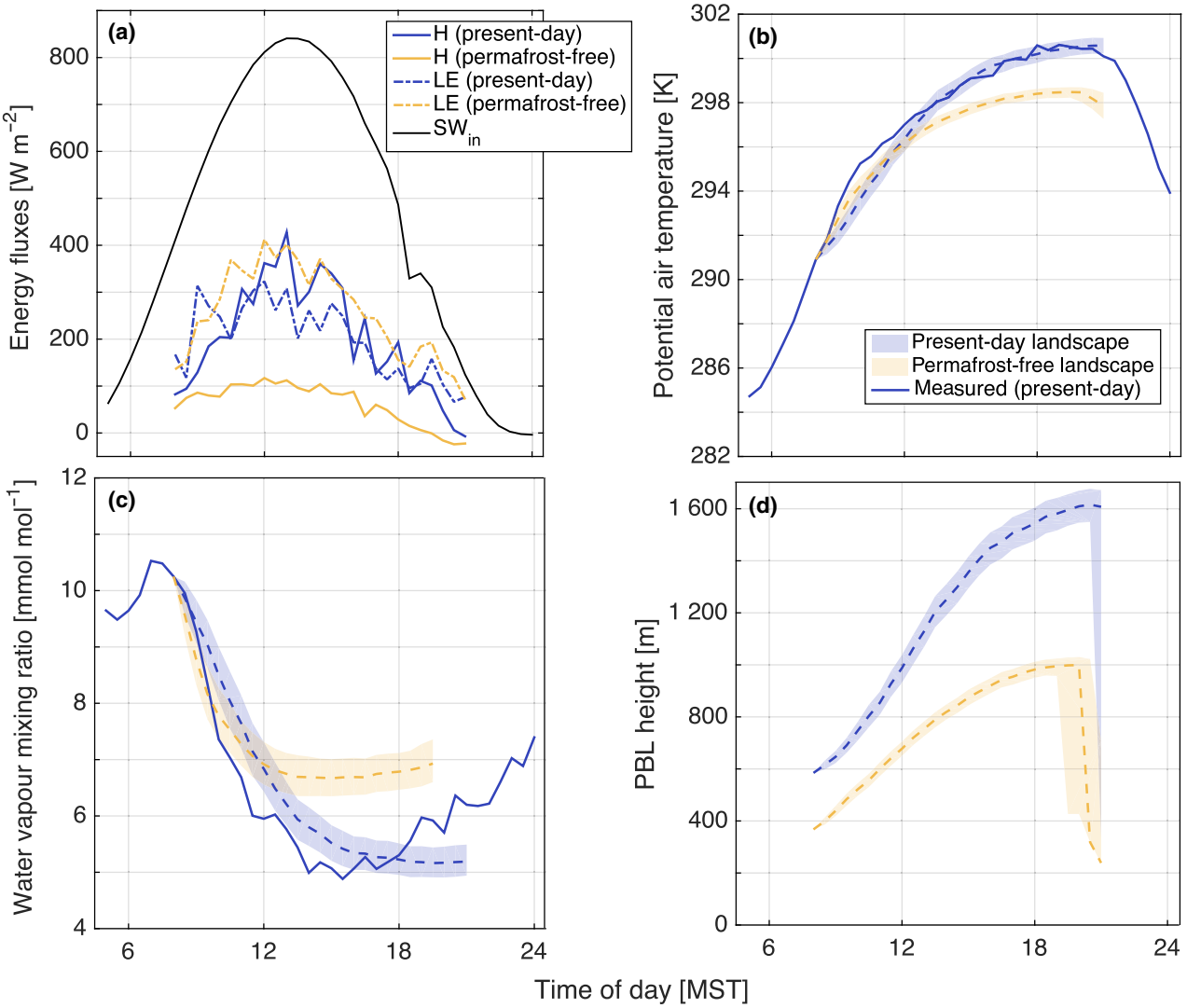

Fig. 8 (a) Sensible (*H*) and latent (*LE*) heat fluxes for a present-day heterogeneous boreal forest–wetland landscape with sporadic permafrost ('present-day landscape') and for a permafrost-free wetland landscape scenario ('permafrost-free landscape') and incoming short-wave radiation (SW_{in}) for 22 June 2014. (b) Measured and modelled potential air temperatures in the mixed layer (θ_m). (c) Measured and modelled water vapour mixing ratios (q_m) and (d) modelled planetary boundary layer (PBL) heights. Shaded areas represent uncertainty due to random errors in flux measurements. q_m is modelled only for the time period before the PBL collapsed.

Vanden Broucke *et al.*, 2015; Stiegler *et al.*, 2016). Here, we combine landscape-scale eddy covariance measurements with regional-scale remote sensing data to quantify an atmospheric cooling and wetting effect of thaw-induced boreal forest loss.

Similar to this study, a decrease of about 50% in annual *H* was observed for a fire-induced transition from a black spruce forest to bunch grasses in Alaska (Liu *et al.*, 2005) with the largest reduction at the end of the winter. In late winter, large albedo increases over treeless wetlands compared to forests drastically reduce available energy following thaw-induced forest-to-wetland conversion. Liquid water is unavailable for *LE* until snow melt, and all available energy is transferred to *H* (Betts *et al.*, 2001). During the summer, differences between boreal forest and wetland albedo are much smaller (e.g. Betts & Ball, 1997). Thus, larger *H* over the forested landscape in the summer is mainly explained by different partitioning of energy between coniferous forests and wetlands (Eugster *et al.*, 2000). Increased post-thaw *LE* and decreased Bowen ratios are consistent with the thaw-induced increase in soil moisture availability (Quinton *et al.*, 2011; Baltzer *et al.*, 2014). A similar thaw-induced change in the partitioning of available energy to *LE* was reported for a tundra ecosystem in northern Sweden (Stiegler *et al.*, 2016). In

temperate and tropical regions, deforestation is generally reducing *LE* (Bala *et al.*, 2007). Similarly, *LE* of a black spruce forest in Alaska decreased during the early treeless postfire regeneration stages (Liu *et al.*, 2005). Thus, impacts of thaw-induced boreal forest loss on land–atmosphere interactions contrast deforestation impacts caused by fire disturbance or clear-cutting due to the associated shift toward higher post-thaw soil moisture.

In contrast to the strong control of wetland coverage on H_{LAND}, the control of wetland coverage on LE_{LAND} is less pronounced, indicating a more complex spatial pattern of water vapour fluxes across the landscape. Transpiration fluxes across the transition from wetlands to forests show a strong spatial heterogeneity (Baltzer *et al.*, 2014; Patankar *et al.*, 2015) and, additionally, *LE* may vary within wetlands due to spatial variations in water table position. In the center of collapse-scar bogs, the water table is deeper due to long-term peat accumulation (Zoltai, 1993; Turetsky *et al.*, 2007). At the recently thawed forest edges, the water table is closest to the moss surface enhancing the *LE* contribution of open water evaporation. In contrast to the landscape tower, these transition zones contributed only little to the wetland tower footprints. The complex spatial patterns in *LE* may reflect these small-scale heterogeneity of surface evaporation sources across boreal forest–wetland landscapes (Brown *et al.*, 2010; Angstmann *et al.*, 2013).

Permafrost thaw and landscape-scale changes in land surface properties

In a well-mixed PBL, atmospheric conditions (e.g. SW_{in}, VPD, T_{air}) over individual wetlands are similar to conditions over the larger boreal forest–wetland landscape, if the surface structure of the landscape is disorganized at length scales <10 km (Shuttleworth, 1988; Garratt, 1994). Thus, contrasts in albedo, and eco-physiological and aerodynamic attributes between permafrost-free ecosystems (wetlands) and ecosystems with permafrost (forests) mainly produce the observed differences in turbulent energy fluxes.

In boreal forests, black spruce stands with low reflectance mask the highly reflective snow or ground cover (e.g. lichen, shrubs) resulting in a lower albedo compared to wetlands. The most pronounced albedo differences occur during the snow cover period when the nonforested ecosystems (e.g. wetlands) are entirely covered by snow. The higher available energy over forest stands (Betts & Ball, 1997; Liu *et al.*, 2005; Lohila *et al.*, 2010; Zhao & Jackson, 2014) indicates that albedo differences mainly induce the thaw-related decrease in *H* during the late winter. In the summer, with smaller albedo contrasts, differences in eco-physiological and aerodynamic properties enhance post-thaw *LE* and attenuate *H*.

Several studies have assessed the land use and land cover change impacts on remotely sensed T_{rs} (e.g. Houspanossian *et al.*, 2013; Zhao & Jackson, 2014; Li *et al.*, 2015). However, T_{as} represents the surface temperature driving *H* and can substantially differ from T_{rs}, particularly in boreal forests with relatively sparse tree density, strong atmospheric coupling of the tree tops, and a ground surface that is more decoupled from the atmosphere (Sun & Mahrt, 1995; Friedl, 2002; Kustas *et al.*, 2006). We suggest that studies of forest loss impacts on remotely sensed T_{rs} should be complemented with analyses of T_{as} (e.g. derived from eddy covariance measurements) to better characterize the effects on local climate (e.g. Baldocchi & Ma, 2013). In this study, we show that thaw-induced forest loss leads to strong late winter cooling of T_{as} and T_{rs}. Summer, cooling of T_{as} instead is moderate, while remotely sensed T_{rs} for the same period indicates a daytime warming effect of forest loss. In contrast to tropical and temperate forests that are affected by large transpirational cooling (Bonan, 2008; Lee *et al.*, 2011), *LE* of black spruce forests is small (Baldocchi *et al.*, 2000). Thus, boreal forests have a minimal transpirational cooling effect (Lee *et al.*, 2011). At the same time, large *LE* over permafrost-free wetlands substantially cools the surface, which explains their lower T_{as} despite lower g_H. Reduced g_H and thus heat transfer efficiency with decreasing forest cover are consistent with lower aerodynamic roughness of low stature ecosystems, such as wetlands, compared to forests (Kelliher *et al.*, 1993; Juang *et al.*, 2007b; Rotenberg & Yakir, 2010).

The thaw-induced decrease in Bowen ratios is mainly caused by increased post-thaw soil moisture (Wright *et al.*, 2009; Baltzer *et al.*, 2014). In addition, the limited stomatal control of *LE* in wetlands, dominated by *Sphagnum* and *Carex* species (Camill, 1999b), favours larger maximum g_s and consequently enhances *LE*. Consistently low g_s is typical for black spruce dominated boreal forests making them more drought resistant compared to other boreal tree species (Baldocchi *et al.*, 2000; Ewers *et al.*, 2005). Additionally, black spruce has a low light-saturation limit of photosynthesis, preventing stomata to open further at higher light levels (e.g. $SW_{in} > 400$ W m^{-2}; Kelliher *et al.*, 1993; Goulden *et al.*, 1997; Dang *et al.*, 1998; Baldocchi *et al.*, 2000). The steady increase of wetland g_s even at high light levels in wetlands may be explained by the forest-wetland differences in soil moisture, their high *Sphagnum* coverage, and their lack of stomata control (Nichols & Brown, 1980; Betts *et al.*, 1999; McFadden

et al., 2003). Similarly, soil moisture limitation on evapotranspiration is reduced and g_s is increased upon thaw in a tundra environment in Sweden (Stiegler *et al.*, 2016).

Regional tree cover controls on surface characteristics

Decreasing tree cover in the southern Taiga Plains favours warmer daytime T_{rs} in summer, contrasting the consistent cooling effect of thaw-induced forest loss on T_{as}. Such a summertime warming effect of forest loss on daytime T_{rs} was previously reported for the boreal zone (Li *et al.*, 2015). Similar to our study, Li *et al.* (2015) found a daytime T_{rs} cooling effect in winter and a year-round cooling effect on night-time T_{rs}. Albedo is most sensitive to tree cover in late winter, when SW_{in} and Bowen ratios are high (Betts *et al.*, 2001; Liu *et al.*, 2005), indicating that albedo differences are the main cause for the observed cooling effect of forest and tree cover loss on T_{rs} (e.g. Betts, 2000; Zhao & Jackson, 2014; Li *et al.*, 2015). In contrast, the warming effect on daytime T_{rs} in the summer is likely caused by eco-physiological and aerodynamic effects exceeding the impacts of smaller summer albedo differences (e.g. Juang *et al.*, 2007b). Transpirational cooling of forests is small and unlikely causing these patterns due to lower *LE* over forests compared to wetlands. To explain the warming effect of tree cover loss on daytime T_{rs} in the summer, we argue that, with increasing tree cover, sensible heat is more efficiently exchanged between the land surface and the atmosphere and ground surface shading is enhanced (e.g. Sun & Mahrt, 1995; Mahrt & Vickers, 2004). The ground surface, which receives less SW_{in} beneath denser canopies due to below-canopy shading (Chasmer *et al.*, 2011a), is strongly affecting remotely sensed T_{rs}. The observed warming effect of tree cover loss on daytime T_{rs} suggests enhanced summertime soil heat input in areas with declining tree cover. This warming effect is consistent with the absence of permafrost in mostly treeless wetlands and the occurrence of permafrost in forested plateaus (Zoltai, 1993; Quinton *et al.*, 2009).

Warmer night-time T_{rs} in densely forested areas may be related to the night-time biomass release of heat storage accumulated during the day (Lindroth *et al.*, 2010). Larger radiative cooling of open- compared to closed-canopy sites was reported for Scotty Creek (Chasmer et al., 2011a). Additionally, forests can be warmer at night because trees reduce the formation of stable stratification allowing a more efficient transport of warm air from above to the surface (Lee *et al.*, 2011). Our results highlight the importance to distinguish between T_{rs} and T_{as} when analysing land cover change impacts and to account for potentially contrasting effects between the snow and snow-free periods as well as between daytime and night-time observations.

Effects of permafrost thaw-induced boreal forest loss on air temperatures and atmospheric moisture

Due to the complex interactions of various biophysical impacts on near-surface climates (Betts *et al.*, 2001), previous studies demonstrated that forest loss appears to have either a cooling or a warming effect on surface air temperature (Juang *et al.*, 2007a,b; Lee *et al.*, 2011; Mildrexler *et al.*, 2011; Alkama & Cescatti, 2016). Lee *et al.* (2011) observed warmer daytime and night-time air temperatures over mid- to high-latitude forests compared to nearby open land due to the combined effects of decreased albedo and increased surface roughness and Bowen ratios. Juang *et al.* (2007b) showed that increased g_H of forests compared to agricultural fields can lead to a cooling effect of afforestation on surface temperature despite concurrent decreases in albedo. On a global scale, a warming effect of forest loss on air temperatures was explained by the decrease in surface roughness and reduced transpirational cooling (e.g. Mildrexler *et al.*, 2011; Alkama & Cescatti, 2016). In this study, we show that thaw-induced boreal forest loss reduces *H* and increases *LE* (i.e. reducing Bowen ratios), exerting a cooling effect on regional air temperature along with an increase in atmospheric moisture.

Reduced diurnal *H* inputs to the PBL over permafrost-free wetlands result in more shallow PBL depths compared to the typically deeper PBL depths characteristic for intact boreal forests (Betts *et al.*, 2001). More shallow PBL depths reduce the effective heat capacity of the PBL (Snyder *et al.*, 2004), generally amplify surface temperature variability (Esau *et al.*, 2012; Davy & Esau, 2014), and, thus, can have profound impacts on regional climates (Esau & Zilitinkevich, 2010). The large diurnal entrainment of warm and dry air into the PBL over boreal forests decreases q_m causing a surface-PBL feedback by further increasing VPD, inducing further decreases in g_s, resulting in enhanced partitioning of available energy to *H*, and eventually further PBL growth (Baldocchi *et al.*, 2000; Hill *et al.*, 2008). However, boreal forest loss and conversion to wetlands with high *Sphagnum* coverage decrease stomata control of *LE*, which could slow down this positive feedback mechanism.

Changes in PBL depth, air temperature and water vapour dynamics may also affect cloud formation and regional precipitation patterns (e.g. Juang *et al.*, 2007b). A decrease in air temperature and a concurrent increase in atmospheric moisture would result in a lower lifting condensation level (height at which condensation of a lifting air parcel occurs) and could potentially increase

cloud cover and the frequency of convective rainfall events (e.g. Betts, 2009). However, as thaw-induced boreal forest loss also leads to decreases in PBL depth, the probability of more frequent convective rainfall events may not increase if the PBL height stays below the lifting condensation level (Juang *et al*., 2007b). Further research using more complex PBL models is required to better characterize the impacts of thaw-induced boreal forest loss on regional precipitation dynamics (e.g. Juang *et al*., 2007b; de Arellano *et al*., 2012).

Permafrost thaw and ultimately its disappearance are likely to continue causing boreal forest loss and wetland expansion in the lowlands of the sporadic permafrost zone in North America. Similar to the southern Taiga Plains, thaw-induced forest loss accelerates in the Tanana Flats in central Alaska. However, there, loss is mainly attributed to decreasing birch forest coverage with a concurrent wetland area increase (Lara *et al*., 2016). The biophysical impacts of deciduous forest loss are likely to differ from the loss of coniferous forests (Juang *et al*., 2007a), even when resulting in similar post-thaw wetland ecosystems. Deciduous forests are generally characterized by a higher albedo, a larger g_s and larger *LE* compared to boreal coniferous forests (Betts & Ball, 1997; Baldocchi *et al*., 2000; Liu *et al*., 2005; Amiro *et al*., 2006). Thus, to better understand how permafrost thaw-induced land cover change affects land–atmosphere interactions and consequently regional and global climates, the biophysical impacts of varying pathways of permafrost thaw need to be assessed in addition to its biogeochemical impacts.

Acknowledgements

The authors are grateful to C. Pappas for discussions improving the manuscript. We thank Dr. C. Hopkinson for providing LiDAR data and E. Houghton for supplying snow density measurements. M. Helbig was funded through graduate student scholarships provided by the Fonds de recherche du Québec – Nature et technologies (FRQNT) and the German Academic Exchange Service (DAAD). Funding for this research was awarded to O. Sonnentag by the Canada Research Chairs, Canada Foundation for Innovation Leaders Opportunity Fund and Natural Sciences and Engineering Research Council Discovery Grant programs. M. Detto was supported by The Forest Global Earth Observatory (ForestGEO). We are grateful for the support of the Liidlii Kue First Nation and Jean-Marie River First Nation for their support of the Scotty Creek Research Station.

References

Alkama R, Cescatti A (2016) Biophysical climate impacts of recent changes in global forest cover. *Science*, **351**, 600–604.

Amiro B, Barr A, Black T *et al*. (2006) Carbon, energy and water fluxes at mature and disturbed forest sites, Saskatchewan, Canada. *Agricultural and Forest Meteorology*, **136**, 237–251.

Angstmann JL, Ewers BE, Barber J, Kwon H (2013) Testing transpiration controls by quantifying spatial variability along a boreal black spruce forest drainage gradient. *Ecohydrology*, **6**, 783–793.

de Arellano JV-G, van Heerwaarden CC, Lelieveld J (2012) Modelled suppression of boundary-layer clouds by plants in a CO_2-rich atmosphere. *Nature Geoscience*, **5**, 701–704.

Aylsworth JM, Kettles IM, Todd BJ (1993) Peatland distribution in the Fort Simpson area, Northwest Territories with a geophysical study of peatland-permafrost relationship at Antoine Lake. In: *Current Research, Part E*, pp. 141–148. Geological Survey of Canada, Paper 93-1E, Ottawa, Canada.

Bala G, Caldeira K, Wickett M, Phillips TJ, Lobell DB, Delire C, Mirin A (2007) Combined climate and carbon-cycle effects of large-scale deforestation. *Proceedings of the National Academy of Sciences of the United States of America*, **104**, 6550–6555.

Baldocchi DD (2014) Measuring fluxes of trace gases and energy between ecosystems and the atmosphere - the state and future of the eddy covariance method. *Global Change Biology*, **20**, 3600–3609.

Baldocchi DD, Ma S (2013) How will land use affect air temperature in the surface boundary layer? Lessons learned from a comparative study on the energy balance of an oak savanna and annual grassland in California, USA. *Tellus Series B*, **65**, 19994.

Baldocchi DD, Kelliher FM, Black TA, Jarvis P (2000) Climate and vegetation controls on boreal zone energy exchange. *Global Change Biology*, **6**, 69–83.

Baltzer JL, Veness T, Chasmer LE, Sniderhan AE, Quinton WL (2014) Forests on thawing permafrost: fragmentation, edge effects, and net forest loss. *Global Change Biology*, **20**, 824–834.

Barr AG, Morgenstern K, Black TA, McCaughey JH, Nesic Z (2006) Surface energy balance closure by the eddy-covariance method above three boreal forest stands and implications for the measurement of the CO_2 flux. *Agricultural and Forest Meteorology*, **140**, 322–337.

Betts RA (2000) Offset of the potential carbon sink from boreal forestation by decreases in surface albedo. *Nature*, **408**, 187–190.

Betts AK (2009) Land-surface-atmosphere coupling in observations and models. *Journal of Advances in Modeling Earth Systems*, **1**, 1–18.

Betts AK, Ball JH (1997) Albedo over the boreal forest. *Journal of Geophysical Research*, **102**, 28901–28909.

Betts AK, Goulden ML, Wofsy SC (1999) Controls on evaporation in a boreal spruce forest. *Journal of Climate*, **12**, 1601–1618.

Betts AK, Ball JH, McCaughey JH (2001) Near-surface climate in the boreal forest. *Journal of Geophysical Research*, **106**, 33529–33541.

Blanken PD, Black TA, Yang PC *et al*. (1997) Energy balance and canopy conductance of a boreal aspen forest: partitioning overstory and understory components. *Journal of Geophysical Research*, **102**, 28915–289267.

Bonan GB (2008) Forests and climate change: forcings, feedbacks, and the climate benefits of forests. *Science*, **320**, 1444–1449.

Bonan GB, Pollard D, Thompson SL (1992) Effects of boreal forest vegetation on global climate. *Nature*, **359**, 716–718.

Brown SM, Petrone RM, Mendoza C, Devito KJ (2010) Surface vegetation controls on evapotranspiration from a sub-humid Western Boreal Plain wetland. *Hydrological Processes*, **24**, 1072–1085.

Camill P (1999a) Peat accumulation and succession following permafrost thaw in the boreal peatlands of Manitoba, Canada. *Écoscience*, **6**, 592–602.

Camill P (1999b) Patterns of boreal permafrost peatland vegetation across environmental gradients sensitive to climate warming. *Canadian Journal of Botany*, **77**, 721–733.

Camill P, Clark JS (1998) Climate change disequilibrium of boreal permafrost peatlands caused by local processes. *The American Naturalist*, **151**, 207–222.

Chapin FS, McGuire AD, Randerson J *et al*. (2000) Arctic and boreal ecosystems of western North America as components of the climate system. *Global Change Biology*, **6**, 211–223.

Chapin FS, Sturm M, Serreze MC *et al*. (2005) Role of land-surface changes in arctic summer warming. *Science*, **310**, 657–660.

Chasmer L, Quinton W, Hopkinson C, Petrone R, Whittington P (2011a) Vegetation canopy and radiation controls on permafrost plateau evolution within the discontinuous permafrost zone, Northwest Territories, Canada. *Permafrost and Periglacial Processes*, **22**, 199–213.

Chasmer L, Kljun N, Hopkinson C *et al*. (2011b) Characterizing vegetation structural and topographic characteristics sampled by eddy covariance within two mature aspen stands using lidar and a flux footprint model: scaling to MODIS. *Journal of Geophysical Research: Biogeosciences*, **116**, G02026.

Chasmer L, Hopkinson C, Veness T, Quinton W, Baltzer J (2014) A decision-tree classification for low-lying complex land cover types within the zone of discontinuous permafrost. *Remote Sensing of Environment*, **143**, 73–84.

Connon RF, Quinton WL, Craig JR, Hayashi M (2014) Changing hydrologic connectivity due to permafrost thaw in the lower Liard River valley, NWT, Canada. *Hydrological Processes*, **28**, 4163–4178.

Dang Q-L, Margolis HA, Collatz GJ (1998) Parameterization and testing of a coupled photosynthesis-stomatal conductance model for boreal trees. *Tree Physiology*, **18**, 141–153.

Davin EL, de Noblet-Ducoudré N (2010) Climatic impact of global-scale deforestation: radiative versus nonradiative processes. *Journal of Climate*, **23**, 97–112.

Davy R, Esau I (2014) Global climate models' bias in surface temperature trends and variability. *Environmental Research Letters*, **9**, 1–8.

Detto M, Montaldo N, Albertson JD, Mancini M, Katul G (2006) Soil moisture and vegetation controls on evapotranspiration in a heterogeneous Mediterranean ecosystem on Sardinia, Italy. *Water Resources Research*, **42**, W08419.

Environment Canada (2014) Canadian Climate Normals: 1981–2010. Available at: http://climate.weather.gc.ca/climate_normals/index_e.html (accessed 23 November 2015).

Esau I, Zilitinkevich S (2010) On the role of the planetary boundary layer depth in the climate system. *Advances in Science and Research*, **4**, 63–69.

Esau I, Davy R, Outten S (2012) Complementary explanation of temperature response in the lower atmosphere. *Environmental Research Letters*, **7**, 044026.

Eugster W, Rouse WR, Pielke RA Sr *et al.* (2000) Land-atmosphere energy exchange in Arctic tundra and boreal forest: available data and feedbacks to climate. *Global Change Biology*, **6**, 84–115.

van Everdingen R (2005) *Multi-Language Glossary of Permafrost and Related Ground-Ice Terms*. National Snow and Ice Data Center, Boulder, CO, 1–90 pp.

Ewers BE, Gower ST, Bond-Lamberty B, Wang CK (2005) Effects of stand age and tree species on canopy transpiration and average stomatal conductance of boreal forests. *Plant, Cell and Environment*, **28**, 660–678.

Fisher JB, Huntzinger DN, Schwalm CR, Sitch S (2014) Modeling the terrestrial biosphere. *Annual Review of Environment and Resources*, **39**, 91–123.

Foken T (2008) The energy balance closure problem: an overview. *Ecological Applications*, **18**, 1351–1367.

Friedl MA (2002) Forward and inverse modeling of land surface energy balance using surface temperature measurements. *Remote Sensing of Environment*, **79**, 344–354.

Garon-Labrecque M-E, Léveillé-Bourret É, Higgins K, Sonnentag O (2015) Additions to the boreal flora of the Northwest Territories with a preliminary vascular flora of Scotty Creek. *Canadian Field-Naturalist*, **129**, 349–367.

Garratt J (1994) Review: the atmospheric boundary layer. *Earth-Science Reviews*, **37**, 89–134.

Goulden ML, Daube BC, Fan S-M, Sutton DJ, Bazzaz A, Munger JW, Wofsy SC (1997) Physiological responses of a black spruce forest to weather. *Journal of Geophysical Research*, **102**, 28987–28996.

Grelle A, Lindroth A, Mölder M (1999) Seasonal variation of boreal forest surface conductance and evaporation. *Agricultural and Forest Meteorology*, **98–99**, 563–578.

Gruber S (2012) Derivation and analysis of a high-resolution estimate of global permafrost zonation. *The Cryosphere*, **6**, 221–233.

Hartmann DL, Klein Tank AMG, Rusticucci M *et al.* (2013) Observations: atmosphere and surface. In: *Climate Change 2013: The Physical Science Basis. Contribution of Working Group I to the Fifth Assessment Report of the Intergovernmental Panel on Climate Change* (eds Stocker TF, Qin D, Plattner G-K, Tignor M, Allen SK, Boschung J, Nauels A, Xia Y, Bex V, Midgley PM), pp. 159–254. Cambridge University Press, Cambridge, UK and New York, NY, USA.

Hayashi M, Goeller N, Quinton WL, Wright N (2007) A simple heat-conduction method for simulating the frost-table depth in hydrological models. *Hydrological Processes*, **21**, 2610–2622.

Helbig M, Pappas C, Sonnentag O (2016) Permafrost thaw and wildfire: equally important drivers of boreal tree cover changes across the Taiga Plains, Canada. *Geophysical Research Letters*, **43**, 1598–1606.

Hill TC, Williams M, Moncrieff JB (2008) Modeling feedbacks between a boreal forest and the planetary boundary layer. *Journal of Geophysical Research*, **113**, D15122.

Houspanossian J, Nosetto M, Jobbágy EG (2013) Radiation budget changes with dry forest clearing in temperate Argentina. *Global Change Biology*, **19**, 1211–1222.

Igarashi Y, Kumagai T, Yoshifuji N *et al.* (2015) Environmental control of canopy stomatal conductance in a tropical deciduous forest in northern Thailand. *Agricultural and Forest Meteorology*, **202**, 1–10.

Jin Y, Randerson JT, Goetz SJ, Beck PSA, Loranty MM, Goulden ML (2012) The influence of burn severity on postfire vegetation recovery and albedo change during early succession in North American boreal forests. *Journal of Geophysical Research: Biogeosciences*, **117**, G01036.

Jorgenson MT, Racine CH, Walters JC, Osterkamp TE (2001) Permafrost degradation and ecological changes associated with a warming climate in central Alaska. *Climatic Change*, **48**, 551–579.

Juang JY, Katul GG, Porporato A *et al.* (2007a) Eco-hydrological controls on summertime convective rainfall triggers. *Global Change Biology*, **13**, 887–896.

Juang JY, Katul G, Siqueira M, Stoy P, Novick K (2007b) Separating the effects of albedo from eco-physiological changes on surface temperature along a successional chronosequence in the southeastern United States. *Geophysical Research Letters*, **34**, L21408.

Kasurinen V, Alfredsen K, Kolari P *et al.* (2014) Latent heat exchange in the boreal and arctic biomes. *Global Change Biology*, **20**, 3439–3456.

Kelliher FM, Leuning R, Schulze ED (1993) Evaporation and canopy characteristics of coniferous forests and grasslands. *Oecologia*, **95**, 153–163.

Kljun N, Rotach MW, Schmid HP (2002) A three-dimensional backward Lagrangian footprint model for a wide range of boundary-layer stratifications. *Boundary-Layer Meteorology*, **103**, 205–226.

Kljun N, Calanca P, Rotach MW, Schmid HP (2004) A simple parameterisation for Flux Footprint Predictions. *Boundary-Layer Meteorology*, **112**, 503–523.

Kljun N, Calanca P, Rotach MW, Schmid HP (2015) A simple two-dimensional parameterisation for Flux Footprint Predictions (FFP). *Geoscientific Model Development*, **8**, 3695–3713.

Kustas WP, Anderson MC, Norman JM, Li F (2006) Utility of radiometric-aerodynamic temperature relations for heat flux estimation. *Boundary-Layer Meteorology*, **122**, 167–187.

Lara MJ, Genet H, McGuire AD *et al.* (2016) Thermokarst rates intensify due to climate change and forest fragmentation in an Alaskan boreal forest lowland. *Global Change Biology*, **22**, 816–829.

Lasslop G, Reichstein M, Kattge J, Papale D (2008) Influences of observation errors in eddy flux data on inverse model parameter estimation. *Biogeosciences*, **5**, 1311–1324.

Lee X, Goulden ML, Hollinger DY *et al.* (2011) Observed increase in local cooling effect of deforestation at higher latitudes. *Nature*, **479**, 384–387.

Li Y, Zhao M, Motesharrei S, Mu Q, Kalnay E, Li S (2015) Local cooling and warming effects of forests based on satellite observations. *Nature Communications*, **6**, 6603.

Lindroth A, Mölder M, Lagergren F (2010) Heat storage in forest biomass improves energy balance closure. *Biogeosciences*, **7**, 301–313.

Liu H, Randerson JT, Lindfors J, Chapin FS (2005) Changes in the surface energy budget after fire in boreal ecosystems of interior Alaska: an annual perspective. *Journal of Geophysical Research: Atmospheres*, **110**, D13101.

Lohila A, Minkkinen K, Laine J *et al.* (2010) Forestation of boreal peatlands: impacts of changing albedo and greenhouse gas fluxes on radiative forcing. *Journal of Geophysical Research*, **115**, G04011.

Luyssaert S, Jammet M, Stoy PC *et al.* (2014) Land management and land-cover change have impacts of similar magnitude on surface temperature. *Nature Climate Change*, **4**, 389–393.

Mahrt L (2000) Surface heterogeneity and vertical structure of the boundary layer. *Boundary-Layer Meteorology*, **96**, 33–62.

Mahrt L, Vickers D (2004) Bulk formulation of the surface heat flux. *Boundary-Layer Meteorology*, **110**, 357–379.

Mauder M, Foken T (2011) *Documentation and Instruction Manual of the Eddy-Covariance Software Package TK3*, pp. 1–60. Univ. Bayreuth, Abt. Mikrometeorologie, Bayreuth, Germany.

McFadden JP, Eugster W, Chapin FS (2003) A regional study of the controls on water vapor and CO_2 exchange in arctic tundra. *Ecology*, **84**, 2762–2776.

McNaughton KG, Spriggs TW (1986) A mixed-layer model for regional evaporation. *Boundary-Layer Meteorology*, **34**, 243–262.

Meissner KJ, Weaver AJ, Matthews HD, Cox PM (2003) The role of land surface dynamics in glacial inception: a study with the UVic Earth System Model. *Climate Dynamics*, **21**, 515–537.

Mildrexler DJ, Zhao M, Running SW (2011) A global comparison between station air temperatures and MODIS land surface temperatures reveals the cooling role of forests. *Journal of Geophysical Research*, **116**, G03025.

Moncrieff JB, Malhi Y, Leuning R (1996) The propagation of errors in long-term measurements of land-atmosphere fluxes of carbon and water. *Global Change Biology*, **2**, 231–240.

Moncrieff JB, Massheder JM, de Bruin H *et al.* (1997) A system to measure surface fluxes of momentum, sensible heat, water vapour and carbon dioxide. *Journal of Hydrology*, **188–189**, 589–611.

Moncrieff J, Clement R, Finnigan J, Meyers T (2004) Averaging, detrending, and filtering of eddy covariance time series. In: *Handbook of Micrometeorology* (eds Lee X, Massman WJ, Law B), pp. 7–31. Springer Netherlands, Amsterdam, The Netherlands.

Nakai T, Kim Y, Busey RC *et al*. (2013) Characteristics of evapotranspiration from a permafrost black spruce forest in interior Alaska. *Polar Science*, **7**, 136–148.
National Wetlands Working Group (1997) *The Canadian Wetland Classification System*, 2nd edn, pp. 1–68, University of Waterloo, Waterloo, ON.
Nichols DS, Brown JM (1980) Evaporation from a Sphagnum moss surface. *Journal of Hydrology*, **48**, 289–302.
Oleson KW, Bonan GB, Levis S, Vertenstein M (2004) Effects of land use change on North American climate: impact of surface datasets and model biogeophysics. *Climate Dynamics*, **23**, 117–132.
Olson DM, Dinerstein E, Wikramanayake ED *et al*. (2001) Terrestrial ecoregions of the world: a new map of life on earth. *BioScience*, **51**, 933–938.
Papale D, Reichstein M, Aubinet M *et al*. (2006) Towards a standardized processing of net ecosystem exchange measured with eddy covariance technique: algorithms and uncertainty estimation. *Biogeosciences*, **3**, 571–583.
Patankar R, Quinton WL, Hayashi M, Baltzer JL (2015) Sap flow responses to seasonal thaw and permafrost degradation in a subarctic boreal peatland. *Trees*, **29**, 129–142.
Quinton WL, Baltzer JL (2013) The active-layer hydrology of a peat plateau with thawing permafrost (Scotty Creek, Canada). *Hydrogeology Journal*, **21**, 201–220.
Quinton WL, Hayashi M, Chasmer LE (2009) Peatland hydrology of discontinuous permafrost in the Northwest Territories: overview and synthesis. *Canadian Water Resources Journal*, **34**, 311–328.
Quinton WL, Hayashi M, Chasmer LE (2011) Permafrost-thaw-induced land-cover change in the Canadian subarctic: implications for water resources. *Hydrological Processes*, **25**, 152–158.
Randerson JT, Liu H, Flanner MG *et al*. (2006) The impact of boreal forest fire on climate warming. *Science*, **314**, 1130–1132.
Rossby CG, Montgomery RB (1935) The layer of frictional influence in wind and ocean currents. *Papers in Physical Oceanography and Meteorology*, **3**, 1–101.
Rotenberg E, Yakir D (2010) Contribution of semi-arid forests to the climate system. *Science*, **327**, 451–454.
Schaepman-Strub G, Schaepman ME, Painter TH, Dangel S, Martonchik JV (2006) Reflectance quantities in optical remote sensing-definitions and case studies. *Remote Sensing of Environment*, **103**, 27–42.
Schmid HP (1997) Experimental design for flux measurements: matching scales of observations and fluxes. *Agricultural and Forest Meteorology*, **87**, 179–200.
Shuttleworth WJ (1988) Macrohydrology - The new challenge for process hydrology. *Journal of Hydrology*, **100**, 31–56.
Snyder PK, Delire C, Foley JA (2004) Evaluating the influence of different vegetation biomes on the global climate. *Climate Dynamics*, **23**, 279–302.
Stiegler C, Johansson M, Christensen TR, Mastepanov M, Lindroth A (2016) Tundra permafrost thaw causes significant shifts in energy partitioning. *Tellus Series B*, **68**, 30467.
Stoy PC, Mauder M, Foken T *et al*. (2013) A data-driven analysis of energy balance closure across FLUXNET research sites: the role of landscape scale heterogeneity. *Agricultural and Forest Meteorology*, **171–172**, 137–152.
Strong WL, Zoltai SC, Ironside G (1989) *Ecoclimatic Regions of Canada* , Ecological edn, Vol. 23. Canadian Wildlife Service, Ottawa, ON.
Sun J, Mahrt L (1995) Relationship of surface heat flux to microscale temperature variations: application to BOREAS. *Boundary-Layer Meteorology*, **76**, 291–301.
Tarnocai C (2006) The effect of climate change on carbon in Canadian peatlands. *Global and Planetary Change*, **53**, 222–232.
Turetsky MR, Wieder RK, Vitt DH, Evans RJ, Scott KD (2007) The disappearance of relict permafrost in boreal north America: effects on peatland carbon storage and fluxes. *Global Change Biology*, **13**, 1922–1934.
Twine TE, Kustas WP, Norman JM *et al*. (2000) Correcting eddy-covariance flux underestimates over a grassland. *Agricultural and Forest Meteorology*, **103**, 279–300.
Van Dijk A, Moene AF, de Bruin HAR (2004) *The Principles of Surface Flux Physics: Theory, Practice and Description of the ECPACK Library, Internal Report 2004/1*. pp. 1–99. Meteorology and Air Quality Group, Wageningen University, Wageningen, The Netherlands.
Vanden Broucke S, Luyssaert S, Davin EL, Janssens I, van Lipzig N (2015) New insights in the capability of climate models to simulate the impact of LUC based on temperature decomposition of paired site observations. *Journal of Geophysical Research: Atmospheres*, **120**, 5417–5436.
Vickers D, Mahrt L (1997) Quality control and flux sampling problems for tower and aircraft data. *Journal of Atmospheric and Oceanic Technology*, **14**, 512–526.
Wan Z (2014) New refinements and validation of the MODIS land-surface temperature/emissivity products. *Remote Sensing of Environment*, **140**, 36–45.
Webb EK, Pearman GI, Leuning R (1980) Correction of flux measurements for density effects due to heat and water vapour transfer. *Quarterly Journal of the Royal Meteorological Society*, **106**, 85–100.
Wilczak JM, Oncley SP, Stage SA (2001) Sonic anemometer tilt correction algorithms. *Boundary-Layer Meteorology*, **99**, 127–150.
Wilson K, Goldstein A, Falge E *et al*. (2002) Energy balance closure at FLUXNET sites. *Agricultural and Forest Meteorology*, **113**, 223–243.
Wohlfahrt G, Haslwanter A, Hörtnagl L, Jasoni RL, Fenstermaker LF, Arnone JA, Hammerle A (2009) On the consequences of the energy imbalance for calculating surface conductance to water vapour. *Agricultural and Forest Meteorology*, **149**, 1556–1559.
Wright N, Hayashi M, Quinton WL (2009) Spatial and temporal variations in active layer thawing and their implication on runoff generation in peat-covered permafrost terrain. *Water Resources Research*, **45**, W05414.
York D, Evensen NM, López M, Delgado JDB (2004) Unified equations for the slope, intercept, and standard errors of the best straight line. *American Journal of Physics*, **72**, 367–375.
Zhao K, Jackson RB (2014) Biophysical forcings of land-use changes from potential forestry activities in North America. *Ecological Monographs*, **84**, 329–353.
Zoltai SC (1993) Cyclic development of permafrost in the peatlands of Northwestern Canada. *Arctic and Alpine Research*, **25**, 240–246.
Zoltai SC, Tarnocai C (1975) Perennially frozen peatlands in the western Arctic and subarctic of Canada. *Canadian Journal of Earth Sciences*, **12**, 28–43.

Appendix 1: Footprint modelling

The 2D flux footprint parameterization of Kljun *et al*. (2015) was applied for the landscape tower for half-hours with roughness lengths smaller than 0.95 m. With larger roughness lengths, the eddy covariance instruments were within the roughness sublayer, where measurements at one fixed point are not representative due to horizontally varying flux magnitudes (Mahrt, 2000). The eddy covariance system at the wetland tower was always above the roughness sublayer. The relative flux contribution matrices were projected on a LiDAR/spectral data fusion-based land cover classification with discrete classes for forests, wetlands and thaw lakes, and a LiDAR-derived canopy height map, both derived from remote sensing (Chasmer *et al*., 2014; Fig. 1c).

Surface energy balance closure at the landscape and the wetland tower

Sums of H and LE measured by the eddy covariance technique were shown to be consistently smaller than available energy (i.e. lack of land surface EBC) across different ecosystems and instrumental set-ups (e.g. Wilson *et al*., 2002; Stoy *et al*., 2013). The reported discrepancies could either be caused by an overestimation of the available energy or an underestimation of turbulent energy fluxes (e.g. Foken, 2008). To ensure the comparability of H and LE at the landscape and the wetland tower, the EBC at the two sites was assessed as follows:

$$H + LE = R_n - G - S - Q_m - C \qquad \text{(A1)}$$

where R_n is net radiation [W m^{-2}], G is the soil heat flux [W m^{-2}], S is the rate of change of heat storage in the air column below the measurement height [W m^{-2}], as derived from one-point changes in T_a and specific

humidity [q_a; kg kg^{-1}], Q_m is the snow melt energy flux [W m^{-2}], and C [W m^{-2}] is the closure term for measurement errors or missing terms (e.g. soil thaw). Heat storage in biomass and the energy flux related to photosynthesis were assumed to be negligible due to the typically low productivity and low biomass of northern boreal forests (Baldocchi *et al.*, 2000; Wilson *et al.*, 2002). No storage term was calculated for the consumption or release of energy for thawing and freezing of the soil above the heat flux plates.

As the flux footprints of the landscape tower mainly consisted of forests and wetlands, the available energy was calculated as a weighted average of the ecosystem-scale measurements of R_n, G, and Q_m at the wetland and the landscape tower. The weights were estimated for each half-hour as the relative contribution of these two land cover types to the flux measurements, quantified with the 2D footprint parameterization of Kljun *et al.* (2015) [see also Chasmer *et al.* (2011b) and Detto *et al.* (2006)].

The EBC for the two towers (defined as the slope of available energy against the sum of turbulent energy fluxes) scale with the contribution of wetlands to the flux measurements, with friction velocity (u_*; m s^{-1}), and soil temperature at 20 cm in the forest (T_{s_FOR}; °C) (Fig. A1). We assume that the relationship of the EBC with T_{s_FOR} is caused by an underestimation of G early in the season due to the omission of a soil thaw energy flux (e.g. Betts *et al.*, 1999; Nakai *et al.*, 2013). In contrast, the dependence of EBC on u_* is likely caused by underestimated H and LE (e.g. Barr *et al.*, 2006). For periods with T_{s_FOR} above 3 °C, u_* above 0.2 m s^{-1} and wetland tower footprint contributions from the wetland larger than 95%, EBC was 0.79 and 0.78 for the landscape and the wetland tower, respectively. We therefore removed flux measurements from both towers when u_* was below 0.2 m s^{-1}, and for the wetland tower when the wetland contribution to the flux footprint was <95% (i.e. footprints extended into surrounding forest). For the landscape tower, data coverage was 50% for H and LE in 2013 (12 May 2013 – 01 November 2013). In 2014 (13 April 2014 – 07 November 2014), data coverage was 52% for H and LE at the landscape tower and 20% for H and LE at the wetland tower.

Atmospheric controls of surface conductance

Nonlinear VPD and SW_{in} models were fitted to g_s for half-hours with low wetland contributions to landscape tower footprints (FR_{WET}) (FR_{WET} < median of FR_{WET} [63%]), to g_s with high FR_{WET} (FR_{WET} ≥ median of FR_{WET} [63%]), and to g_s derived from fluxes at the wetland tower (contributions from wetlands ≥95%). Only daytime g_s (0900 and 2100 MST) and g_s for periods with LE >10 W m^{-2} were used, as the expression of g_s becomes numerically unstable when LE <10 W m^{-2}. The VPD control on G_{s_bound} was modelled as follows (e.g. Blanken *et al.*, 1997):

$$G_{s\_bound\_i} = g_{s0\_i}\, e^{(-b_d \mathrm{VPD})} \tag{A2}$$

where i stands for the i-th data set class, g_{s_0} (m s^{-1}) is the bulk surface conductance at a VPD of 0 kPA, and b_d indicates the sensitivity of G_{s_bound} to VPD (kPa^{-1}). The model was fitted to the upper 15% of g_s per 0.5 kPa VPD window. Data for periods with SW_{in} <300 W m^{-2} were excluded to avoid radiation-controlled g_s.

The dependence of G_{s_bound} on SW_{in} was modelled using a Michaelis–Menten function (e.g. Grelle *et al.*, 1999):

$$G_{s\_bound\_i} = g_{s\_max\_i}\, \frac{SW_{in}}{b_{infl} + SW_{in}} \tag{A3}$$

where g_{s_max} is the upper limit of g_s at high SW_{in} and b_{infl} is a parameter defining SW_{in} when G_{s_bound} reaches half of its upper limit. To assess the radiation dependence of G_{s_bound}, only periods with VPD >0.3 kPa were analysed ensuring that g_s was not controlled by VPD. Uncertainties of the model fits were quantified by fitting the model to 1000 bootstrap realizations of the data sets.

The planetary boundary layer model

The time rate of change in potential air temperature of the mixed layer ($\frac{d\theta_m}{dt}$; K s^{-1}) results from input of sensible heat from the surface (H) and from entrainment of warm air above the temperature inversion at the top of the mixed layer and was modelled using Eqn. 1 in McNaughton & Spriggs (1986). The time rate of change in q_m was calculated using Eqn. 2 in McNaughton & Spriggs (1986). Eqn. 10 in McNaughton & Spriggs (1986) was used to model the time rate of change in PBL height:

$$\frac{dh}{dt} = \frac{H_v}{\rho C_p h \Gamma_v} \tag{A4}$$

The vertical gradient of virtual potential air temperature [lapse rate (Γ_v); K m^{-1}] was taken as the lapse rate of moist air of 0.0065 K m^{-1}.

To model q_m at the landscape tower, we used H and LE from the landscape tower as forcing. Modelled θ_m and q_m can only be compared to measured θ_m and q_m when H and LE at the landscape tower are representative of the energy fluxes affecting instantaneous PBL

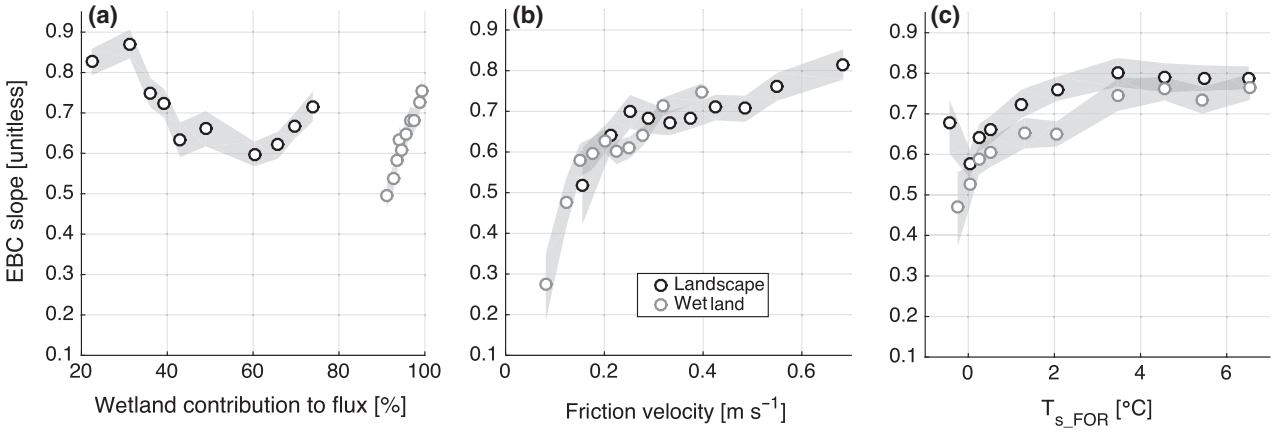

Fig. A1 Slope of the energy balance closure (EBC) for the landscape and the wetland tower as function of (a) permafrost-free wetland contributions to flux footprints, (b) friction velocity, and (c) soil temperature at 20 cm on the forested permafrost plateau (T_{s_FOR}). Shaded areas show the 95% confidence interval of the slopes.

dynamics, which is not always the case over a heterogeneous landscape. We included only days with clear-sky conditions and a total sum of less than five half-hours of missing or low quality (quality flag >1) H and LE at the landscape and the wetland tower. Remaining gaps were filled using linear interpolation and days with an RMSE of the modelled θ_m >2 K were discarded to ensure good model performance. The analysis of the EBC indicated an average underestimation of ~20% of the sum of H and LE (see above). Therefore, we corrected for this underestimation in our model by increasing the measured H and LE accordingly assuming that the lack of EBC was equally caused by H and LE (Twine *et al*., 2000; Wohlfahrt *et al*., 2009).

Air temperature and water vapour mixing ratio at Scotty Creek were only measured in the mixed layer and, thus, θ_e and q_e were not known. Potential air temperature and q_e of the entrainment layer were derived numerically by minimizing the RMSE of modelled θ_m and q_m versus measured θ_m and q_m at the landscape tower. Friction velocity was used to calculate the initial PBL height (Rossby & Montgomery, 1935).

Supporting Information

Additional Supporting Information may be found in the online version of this article:

Data S1. Derivation of roughness parameters and aerodynamic conductance.
Figure S1. Seasonal dynamics of soil temperature, water table relative to moss surface, and snow depth in 2014 in the (a) wetland and in the (b) boreal forest at Scotty Creek.
Figure S2. Pictures of the studied wetland in Scotty Creek in the (a) late winter, (b) spring, (c) summer, and (d) fall of 2014.
Figure S3. Aerodynamic roughness length for momentum and LIDAR-derived mean weighted canopy height within flux footprints between May and September 2013 and 2014.
Figure S4. Mean diurnal averages of radiometric (T_{rs}) and aerodynamic (T_{as}) surface temperature for the (a, c, e) late winter and (b, d, f) the snow-free period in 2014 for (a, b) the wetland and (c, d) the forest (i.e. T_{rs}) and the heterogeneous landscape (i.e. T_{as}).
Figure S5. Random uncertainty in sensible heat (H; a-b) and latent heat flux measurements (LE; c-d) for the landscape (a, c) and the wetland tower (b, d) derived after Lasslop *et al*. (2008).

